

Summer 2018

MATERIAL PROPERTIES OF LASER POWDER BED FUSION PROCESSED 316L STAINLESS STEEL

Steven Keckler
Montana Tech

Follow this and additional works at: https://digitalcommons.mtech.edu/grad_rsch



Part of the [Metallurgy Commons](#)

Recommended Citation

Keckler, Steven, "MATERIAL PROPERTIES OF LASER POWDER BED FUSION PROCESSED 316L STAINLESS STEEL" (2018). *Graduate Theses & Non-Theses*. 182.
https://digitalcommons.mtech.edu/grad_rsch/182

This Thesis is brought to you for free and open access by the Student Scholarship at Digital Commons @ Montana Tech. It has been accepted for inclusion in Graduate Theses & Non-Theses by an authorized administrator of Digital Commons @ Montana Tech. For more information, please contact sjuskiewicz@mtech.edu.

MATERIAL PROPERTIES OF LASER POWDER BED FUSION
PROCESSED 316L STAINLESS STEEL

by
Steven Keckler

A thesis submitted in partial fulfillment of the
requirements for the degree of

Master of Science in Metallurgical and Mineral Processing Engineering

Montana Technological University

2018



Abstract

Laser powder bed fusion additive manufactured 316L stainless steel specimens were evaluated to establish a baseline for future research in determining an optimized energy density and build orientation. Test specimens were printed at various energy densities. At each energy density, tensile and fatigue specimens were printed at 0° (longitudinal), 45°, and 90° (transverse) orientation to the build plate. Tensile and high cycle fatigue tests were performed then representative fracture surfaces were analyzed. The apparent melt track and dendrite size were evaluated using grain analysis software. Static loading of the tensile specimens showed a marginal difference in UTS for specimens with a longitudinal and 45° orientation to the build plate. The transverse orientation was more variable due to the UTS response to the quality of fusion between melt track layers. The energy density affected the fatigue as well. Typically, the medium energy density had the most consistent behavior. Fractography revealed a relationship between energy density and melt track fusion. The optimum energy density in this study was determined to be 100 J/mm³, based on the highest transverse UTS, highest fatigue limit, moderate ductility, and moderate volume of lack of fusion defects. Specimens fabricated at a lower energy density had insufficient heat input to achieve good fusion which reduced the transverse UTS, ductility, and fatigue limit. The highest energy density was excessive energy density leading to an increase in defects reducing the transverse UTS and fatigue limit. The UTS was not strongly affected by the defect volume except in the transverse orientation, where a high defect volume reduced the quality of fusion between melt track layers.

Keywords: Additive Manufacturing, Laser powder bed fusion, 316L stainless steel, fractography

Dedication

First and foremost, I dedicate this work to my beloved wife, who without her constant love and support, this work would have been impossible. Beyond my wife, without the continued support of my family and close friends, it would have made this work much more difficult to accomplish.

Acknowledgements

I would like to begin by thanking the Army Research Laboratory for their financial support in this study.

Many thanks to my graduate committee: Dr. K.V. Sudhakar, Dr. Ronald White, Dr. Bruce Madigan, and Ronda Coguill.

Thank you to Ronda Coguill and Taylor Winsor for performing the mechanical testing for the study. Further, I wish to thank Ryan Foley and my undergraduates, Benjamin Suslavich and Avery Flanik, for their aid in completing the microstructural analysis.

My unending gratitude is to Chirre Keckler, Emily Moses Keckler, and Ronda Coguill for their aid in editing this report.

Thank you to my fellow graduate students Penn Rawn, Edward Stugelmayer, Luke Suttey, and Ryan Foley for their aid, insight, and support in performing this study.

Research was sponsored by the Army Research Laboratory and was accomplished under Cooperative Agreement Number W911NF-15-2-0020. The views and conclusions contained in this document are those of the authors and should not be interpreted as representing the official policies, either expressed or implied, of the Army Research Laboratory or the U.S. Government. The U.S. Government is authorized to reproduce and distribute reprints for Government purposes notwithstanding any copyright notation herein.

Table of Contents

ABSTRACT	II
DEDICATION	III
ACKNOWLEDGEMENTS	IV
LIST OF TABLES.....	VII
LIST OF FIGURES.....	XI
LIST OF EQUATIONS	XVI
GLOSSARY OF TERMS	XVII
1. INTRODUCTION.....	1
1.1. 316L Stainless Steel	2
1.2. Selective Laser Melting	2
1.2.1. Melt Track Formation	4
1.2.2. Melt Track Solidification.....	4
1.2.2.1. Microstructures Observed	5
1.2.3. Mechanical Properties.....	6
1.3. Notable Factors Effecting SLM.....	7
1.3.1. Powder Properties.....	8
1.3.2. Energy Density.....	9
1.3.3. Atmosphere.....	11
1.3.4. Commonly Observed LPBF Defects	12
1.3.5. Post Processing Techniques	14
2. RESEARCH OBJECTIVES	15
3. METHODOLOGY	16
3.1. Material and Specimen Creation.....	16
3.2. Tensile Testing.....	17
3.3. Fatigue Testing.....	17

3.4.	<i>Fractography</i>	18
3.5.	<i>Microstructural Analysis</i>	18
4.	RESULTS	20
4.1.	<i>Ultimate Tensile Strength</i>	20
4.2.	<i>High Cycle Fatigue</i>	21
4.3.	<i>Fractography</i>	24
4.3.1.	Low Energy Density Tensile Fractography	25
4.3.2.	Medium Energy Density Tensile Fractography	29
4.3.3.	High Energy Density Tensile Fractography	33
4.3.4.	Low Energy Density Fatigue Fractography	36
4.3.5.	Medium Energy Density Fatigue Fractography	39
4.3.6.	High Energy Density Fatigue Fractography.....	43
4.4.	<i>Microstructural Analysis</i>	46
5.	DISCUSSION	49
5.1.	<i>Ultimate Tensile Strength</i>	49
5.2.	<i>High Cycle Fatigue</i>	49
5.3.	<i>Fractography</i>	50
5.4.	<i>Microstructural Analysis</i>	51
6.	CONCLUSIONS.....	52
7.	RECOMENDATIONS.....	54
8.	REFERENCES.....	55
9.	APPENDIX A: TABULATED MECHANICAL TEST RESULTS.....	60
10.	APPENDIX B: EXAMPLE DRAWING OF MODERATE DUCTILITY TENSILE FRACTURE.....	61
11.	APPENDIX C: TABULATED STATISTICS FOR APPARENT MELT TRACK SIZE	62
12.	APPENDIX D: TABULATED STATISTICS FOR DENDRITE SIZE	69

List of Tables

Table I: Chemical composition of 316L stainless steel [3].....	2
Table II: Chemical composition of stainless steel powder used for construction of AM components.	16
Table III: Process variables and energy densities for the sets of test specimens constructed.	17
Table IV: Tabulated Average UTS Results	60
Table V: Tabulated Fatigue Test Results.....	60
Table VI: Low energy density 0° orientation apparent melt track area, length, and breadth statistics for the ‘XY’ sample.	62
Table VII: Low energy density 0° orientation apparent melt track area, length, and breadth statistics for the ‘Z’ sample.....	62
Table VIII: Low energy density 45° orientation apparent melt track area, length, and breadth statistics for the ‘XY’ sample.	63
Table IX: Low energy density 45° orientation apparent melt track area, length, and breadth statistics for the ‘Z’ sample.....	63
Table X: Low energy density 90° orientation apparent melt track area, length, and breadth statistics for the ‘XY’ sample.	63
Table XI: Low energy density 90° orientation apparent melt track area, length, and breadth statistics for the ‘Z’ sample.....	64
Table XII: Medium energy density 0° orientation apparent melt track area, length, and breadth statistics for the ‘XY’ sample.	64

Table XIII: Medium energy density 0° orientation apparent melt track area, length, and breadth statistics for the ‘Z’ sample.....	64
Table XIV: Medium energy density 45° orientation apparent melt track area, length, and breadth statistics for the ‘XY’ sample.	65
Table XV: Medium energy density 45° orientation apparent melt track area, length, and breadth statistics for the ‘Z’ sample.....	65
Table XVI: Medium energy density 90° orientation apparent melt track area, length, and breadth statistics for the ‘XY’ sample.	65
Table XVII: Medium energy density 90° orientation apparent melt track area, length, and breadth statistics for the ‘Z’ sample.....	66
Table XVIII: High energy density 0° orientation apparent melt track area, length, and breadth statistics for the ‘XY’ sample.	66
Table XIX: High energy density 0° orientation apparent melt track area, length, and breadth statistics for the ‘Z’ sample.....	66
Table XX: High energy density 45° orientation apparent melt track area, length, and breadth statistics for the ‘XY’ sample.	67
Table XXI: High energy density 45° orientation apparent melt track area, length, and breadth statistics for the ‘Z’ sample.....	67
Table XXII: High energy density 90° orientation apparent melt track area, length, and breadth statistics for the ‘XY’ sample.	67
Table XXIII: High energy density 90° orientation apparent melt track area, length, and breadth statistics for the ‘Z’ sample.....	68

Table XXIV: Low energy density 0° orientation dendrite area, length, and breadth statistics for the ‘XY’ sample.....	69
Table XXV: Low energy density 0° orientation dendrite area, length, and breadth statistics for the ‘Z’ sample.	69
Table XXVI: Low energy density 45° orientation dendrite area, length, and breadth statistics for the ‘XY’ sample.....	69
Table XXVII: Low energy density 45° orientation dendrite area, length, and breadth statistics for the ‘Z’ sample.	70
Table XXVIII: Low energy density 90° orientation dendrite area, length, and breadth statistics for the ‘XY’ sample.	70
Table XXIX: Low energy density 90° orientation dendrite area, length, and breadth statistics for the ‘Z’ sample.	70
Table XXX: Medium energy density 0° orientation dendrite area, length, and breadth statistics for the ‘XY’ sample.	71
Table XXXI: Medium energy density 0° orientation dendrite area, length, and breadth statistics for the ‘Z’ sample.....	71
Table XXXII: Medium energy density 45° orientation dendrite area, length, and breadth statistics for the ‘XY’ sample.	71
Table XXXIII: Medium energy density 45° orientation dendrite area, length, and breadth statistics for the ‘Z’ sample.....	72
Table XXXIV: Medium energy density 90° orientation dendrite area, length, and breadth statistics for the ‘XY’ sample.	72

Table XXXV: Medium energy density 90° orientation dendrite area, length, and breadth statistics for the 'Z' sample.....	72
Table XXXVI: High energy density 0° orientation dendrite area, length, and breadth statistics for the 'XY' sample.....	73
Table XXXVII: High energy density 0° orientation dendrite area, length, and breadth statistics for the 'Z' sample.....	73
Table XXXVIII: High energy density 45° orientation dendrite area, length, and breadth statistics for the 'XY' sample.	73
Table XXXIX: High energy density 45° orientation dendrite area, length, and breadth statistics for the 'Z' sample.....	74
Table XL: High energy density 90° orientation dendrite area, length, and breadth statistics for the 'XY' sample.....	74
Table XLI: High energy density 90° orientation dendrite area, length, and breadth statistics for the 'Z' sample.	74

List of Figures

Figure 1: General Schematic of LPBF process.....	3
Figure 2: Image of Specimen on build plate. Arrow points to support structure.....	5
Figure 3: Image of an EOS M29 Printer [41]	16
Figure 4: 'XY' and 'Z' sample orientations.....	19
Figure 5: Average UTS of specimens studied.	21
Figure 6: Low Energy Density (55.6J/mm ³) Fatigue Test Results	22
Figure 7: Medium Energy Density (100.0 J/mm ³) Fatigue Test Results.....	23
Figure 8: High Energy Density (187.6 J/mm ³) Fatigue Test Results	24
Figure 9: 55.6 J/mm ³ energy density 0° orientation tensile fracture surface. Predominantly ductile failure mode with a flat fracture surface.....	25
Figure 10: 55.6 J/mm ³ energy density 0° orientation tensile fracture surface. Fracture surface is mix of high ductility and moderate ductility features. Moderate ductility material is determined by the presence of dimpling and fine spherical porosity; see region A. Areas lacking fine dimpling but still with indication of plastic flow are a low ductility; see region B. Arrow C points to a moderate sized shallow void.	26
Figure 11: 55.6 J/mm ³ energy density at the 0° for Frame 1, and 45°, Frames 2 and 3, tensile fracture surfaces. Frame 1: Example of brittle features distributed across the failure surface and are identified by angular fracture surfaces. Frame 2: Angular void with brittle features such as secondary cracking (arrow indicates) and angular surfaces, A. To right of void is a partially fused powder particle, B, in a region of moderate ductility. Frame 3: Clump of partially fused powder particles with brittle features, arrow indicates. .	27

- Figure 12: 55.6 J/mm³ energy density 90° orientation tensile fracture. Fracture surface that broke between layers of melt tracks. Individual melt tracks are identifiable and poorly fused to each other.28
- Figure 13: 55.6 J/mm³ energy density 90° orientation tensile fracture. Poorly fused melt tracks and powder particles.29
- Figure 14: 100.0 J/mm³ energy density 0° orientation tensile fracture. Ductile failure mode with well-developed shear lips. Ductile tearing at the base of the shear lips and central area of fracture surface. Moderate distribution of irregular pores across the fracture surface.30
- Figure 15: 100.0 J/mm³ energy density 0° orientation tensile fracture. Honey comb structure with irregular voids observed to have lack of fusion defects (A arrows) at their base and ribbing that traversed the interior of the void the entire length. B arrow points to area of brittle features31
- Figure 16: 100.0 J/mm³ energy density 0° orientation tensile fracture. Predominantly ductile failure mode with a flat fracture surface and high volume of voids.32
- Figure 17: 100.0 J/mm³ energy density 45° orientation tensile fracture. Example of angular brittle voids observed distributed across the specimen surface.....32
- Figure 18: 100.0 J/mm³ energy density 90° orientation tensile fracture. Ductile failure mode with well-developed shear lips. Ductile tearing at the base of the shear lips and central area of fracture surface. Moderate distribution of irregular pores across the fracture surface.33
- Figure 19: 187.6 J/mm³ energy density 0° orientation tensile fracture. Ductile failure mode with well-developed shear lips, ductile tears and low distribution of irregular voids. ...34

- Figure 20: 187.6 J/mm³ energy density 45° orientation tensile fracture. Honey comb structure with an irregular void possessing a rind of brittle material.35
- Figure 21: 187.6 J/mm³ energy density 90° orientation tensile fracture. Honey comb structure with a smooth walled circular void.....35
- Figure 22: 55.6 J/mm³ energy density 0° orientation fatigue fracture. Red arrows point to pair of crack initiation sites. Enclosed is large lack of fusion defect where most of lower crack propagation occurred. Red line traces approximate end of crack propagation zone.36
- Figure 23: 55.6 J/mm³ energy density 0° orientation fatigue fracture. Brittle fast fracture and final fracture zone. Final fracture zone identifiable to flat planar fracture surface, red arrow indicates.37
- Figure 24: 55.6 J/mm³ energy density 45° orientation fatigue fracture. Red arrow in magnified image points to lack of fusion defect from which crack initiation occurred. The approximate transition point between the crack initiation zone and fast fracture zone is outlined in the magnified image. A high volume of irregular shaped voids is observed in the first third of fast fracture zone, enclosed in oval.....38
- Figure 25: 55.6 J/mm³ energy density 90° orientation fatigue fracture. Red arrow points to crack initiation site, a small surface defect. Crack broke over to a large lack of fusion defect center of crack propagation zone, enclosed in oval.39
- Figure 26: 100.0 J/mm³ energy density 0° orientation fatigue fracture. In magnified image red arrow points to crack initiation site, a small surface defect. Transition from crack propagation to fast fracture is outlined.40
- Figure 27: 100.0 J/mm³ energy density 45° orientation fatigue fracture. In magnified image red arrow points to crack initiation site, a small surface defect, which broke over to a large

- lack of fusion defect, A. Crack propagation zone is a non-typical shape, an approximate oval, enclosed in oval.....41
- Figure 28: 100.0 J/mm³ energy density 90° orientation fatigue fracture. Magnified image highlights complex of crack initiation sites along specimen edge and first portion of crack propagation zone.42
- Figure 29: 100.0 J/mm³ energy density 90° orientation fatigue fracture. Transition zone between crack propagation zone and fast fracture zone approximately outlined. Arrow indicates direction of crack propagation.42
- Figure 30: 187.6 J/mm³ energy density 0° orientation fatigue fracture. Red arrows point to a pair of adjacent crack initiation sites. Initiation site A is a small surface defect, site B a large surface defect, outer surface is magnified. Approximate end of crack propagation zone is outlined.43
- Figure 31: 187.6 J/mm³ energy density 0° orientation fatigue fracture. Final fracture zone with brittle features along cleavage planes. Arrow in magnified image is a large irregular shaped void.44
- Figure 32: 187.6 J/mm³ energy density 45° orientation fatigue fracture. Red arrow points toward a surface feature reminiscent of striations but in a direction perpendicular to expected direction.45
- Figure 33: 187.6 J/mm³ energy density 45° orientation fatigue fracture. Proposed final fracture zone indicated by transition to flat planar fracture surface lacking striations.45
- Figure 34: 187.6 J/mm³ energy density 90° orientation fatigue fracture. Red arrow in magnified image points to surface defect which initiated cracking. Line traces approximate end of crack propagation zone.46

Figure 35: Mean apparent melt track area and standard deviation for the low, medium, and high energy densities.....47

Figure 36: Mean dendrite area and standard deviation for the low, medium, and high energy densities.....48

Figure 37: Example cross section diagram of a moderate ductility tensile fracture.61

List of Equations

Equation 1: Formula for the calculation of volumetric energy density.	10
Equation 2: Formula for the calculation moment for fatigue testing using a Fatigue Dynamics Inc. RBF-200. [42]	18

Glossary of Terms

Term	Definition
Additive Manufacturing* (AM)	A process of joining materials to make objects from 3D model data, usually layer upon layer, as opposed to subtractive manufacturing methodologies. Synonyms: additive fabrication, additive processes, additive techniques, additive layer manufacturing, layer manufacturing, and freeform fabrication.
Energy Density	Heat input to the system over a unit area or volume.
Hatch Spacing	The distance between the center of two melt tracks
HIP	Hot Isostatic Pressing
Melt Track	The line of molten or previously molten material. Melt tracks are akin to a weld bead.
Powder Bed Fusion* (PBF)	An additive manufacturing process in which thermal energy selectively fuses regions of a powder bed.
LPBF	Laser Powder Bed Fusion
Marangoni Flow	Mass transfer of fluid due to a gradient in surface tension
Subtractive Manufacturing*	Making objects by removing of material (for example, milling, drilling, grinding, carving, etc.) from a bulk solid to leave a desired shape, as opposed to additive manufacturing.
SEM	Scanning Electron Microscope
Selective Laser Melting (SLM)	An additive manufacturing process where metallic powder is fused together to form components based on a 3D CAD file
UTS	Ultimate Tensile Strength

*Definition quoted from ASTM standard: F2792–12a.

1. INTRODUCTION

Additive manufacturing (AM) has its roots in the use of polymers to create rapid prototyped components for research and development applications with the first commercially viable units going to market in 1987 [1]. In recent years, advancements have been made to commercial production of metallic AM components [2-5]. Selective laser melting (SLM) now produces components constructed with a dimensional accuracy on par with precision casting [6], and possess mechanical properties comparable to wrought components [7]. Aerospace, automotive, and biomedical fields were among the early adopters of AM processes [8].

Currently, AM is relegated to niche usage for components and applications that have low production volumes and complex geometries, mainly due to cost of production. AM benefits from the ability to design and produce components with optimized preproduction steps as compared to traditional manufacturing. This includes the ability to design new components faster and without tooling to design or fabricate. AM has other production benefits, including a smaller equipment footprint and less material waste compared to subtractive manufacturing [4, 5]. Standardized methods are still under development for component design and construction for AM. To accomplish this, information needs to be assembled, analyzed, and implemented for powder composition and the effect of process variables. Databases need are being built from investigations of previously unknown methods to produce optimized components. [2, 8].

The AM process can be generally broken down into the following steps. (1) Components are designed using a 3D computer assisted design program. (2) The design is then put into standard tessellation language and sliced into layers which correspond with the layer thickness that will be deposited during construction. (3) Once in this format, the file can be sent to an AM unit where it will be printed in a layerwise fashion. (4) After construction is completed, the

component is removed from the unit. The component can either be put directly into service or undergo a wide variety of post processing operations such as heat treatment or machining.

1.1. 316L Stainless Steel

The material chosen for analysis in this study was 316L stainless steel. It is an austenitic grade of stainless steel with a moderate chromium and relatively high nickel content. The range of compositions that describe 316L stainless steel is listed in Table I. 316L stainless steel has shown positive results in previous studies on SLM [3-6, 9-22], and has seen wide application in the aerospace and biomedical fields. One of the primary benefits of 316L stainless steel for SLM is its good weldability. This benefit derives from its resistance to hot and cold cracking due to its low carbon and moderate molybdenum content.

Table I: Chemical composition of 316L stainless steel [3].

Element	Wt. %
Cr	16 - 18
Ni	10 - 14
Mo	2 - 3
C	< 0.03
Si	< 1
Mn	< 2
P	< 0.045
S	< 0.03
N	< 0.1
Fe	Balance

1.2. Selective Laser Melting

SLM is a branch of AM that utilizes a laser as the heat source for fusion. SLM is functionally laser welding on the microscopic scale that produces melt pools with a high aspect ratio and a small heat effected zone [23]. Within this family of AM processes, selective laser melting (SLM) is a subset in which the material to be fused reaches a total liquid state during the printing process. SLM processes have demonstrated the ability to produce components with greater than 99% densification and geometries that were unobtainable using traditional

manufacturing techniques [25]. Given the ability for SLM components to be designed with custom tailored geometries and microstructures, there has been new momentum adoption of this type of AM processing [18, 24].

The most common method of SLM is laser powder bed fusion (LPBF) [5, 14], a specific manufacturing process under the umbrella of SLM. LPBF prints components in a layerwise fashion where a thin layer of powder is deposited, followed by the laser tracing a 2D contour. Powder deposition and lasing is repeated until the component is completed, depicted Figure 1.

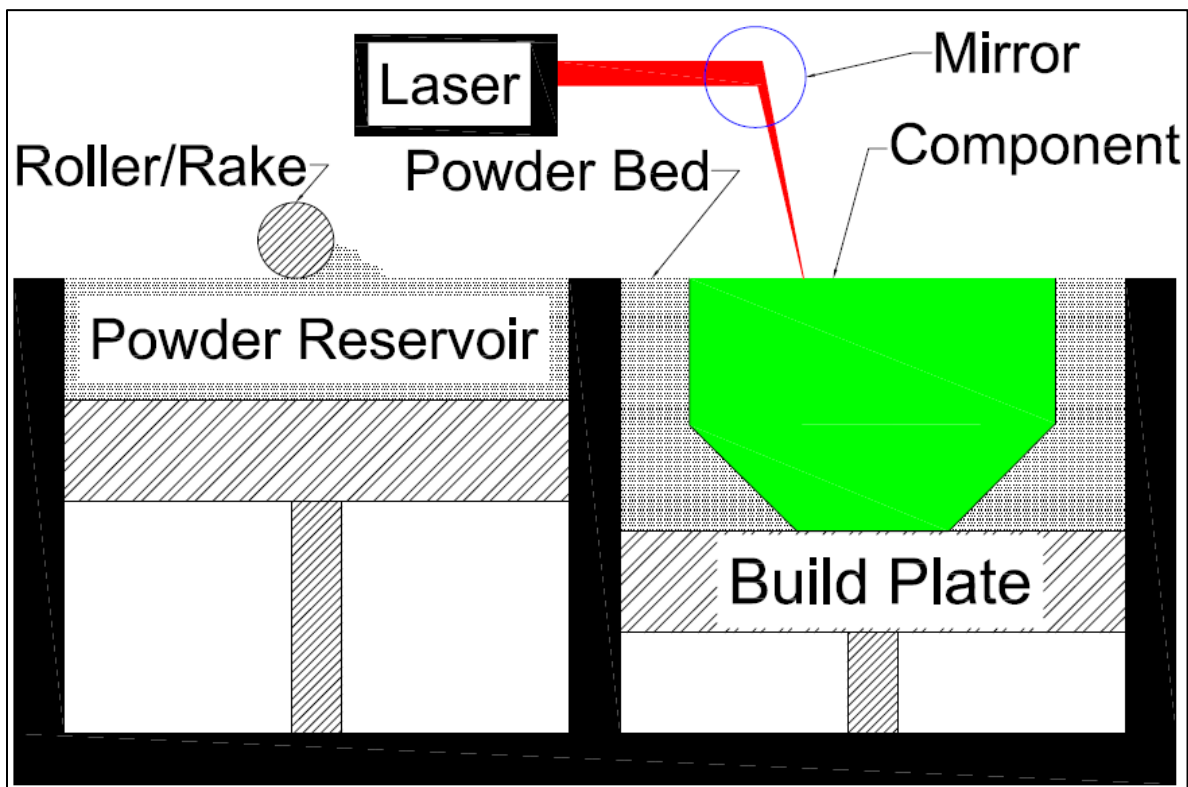


Figure 1: General Schematic of LPBF process

SLM involves many complex facets that have significant effects on component behavior. Melt track formation and solidification forms the basis of component properties. Solidification of the material controls what type of microstructure will form and by extension the mechanical properties.

1.2.1. Melt Track Formation

Heat input is determined by the laser power. Scan speed controls the melting rate, cooling rate, and contributes strongly to melt track stability. Heat input to the metal powder is estimated to be as high as 10^7 K/s [2]. The heat transferred to the metal powder is often low compared to the laser power due to high reflectivity [23]. LPBF is generally operated at an energy density that facilitates conduction mode melting. In this type of melt process, the laser only directly interacts with the top surface of the powder bed which, within microseconds, receives sufficient heat to transition to a liquid state. Once the material transitions to a liquid state, capillary action is the rate controlling step for melt pool formation. Capillary action pulls the liquid into the powder bed bringing in more powder particles, thus establishing the melt pool size [2]. As the laser travels along its scan path, a melt track is formed akin to welding.

1.2.2. Melt Track Solidification

During solidification the cooling rate can exceed 10^6 K/s [5, 6, 9, 24]. Rapid cooling induces non-equilibrium solidification, in conjunction with Marangoni flow, which leads to refined grains with minimal alloy segregation. As successive layers of melt tracks are deposited, the size of the melt tracks increases and the cooling rate decreases [17]. The cooling rate promotes a residual stress great enough to make it often necessary for components to be constructed with extra supports to prevent warping; example of support is presented in Figure 2. The residual stress is affected by energy density, scan regime, and component geometry [5, 6, 9, 24-27].

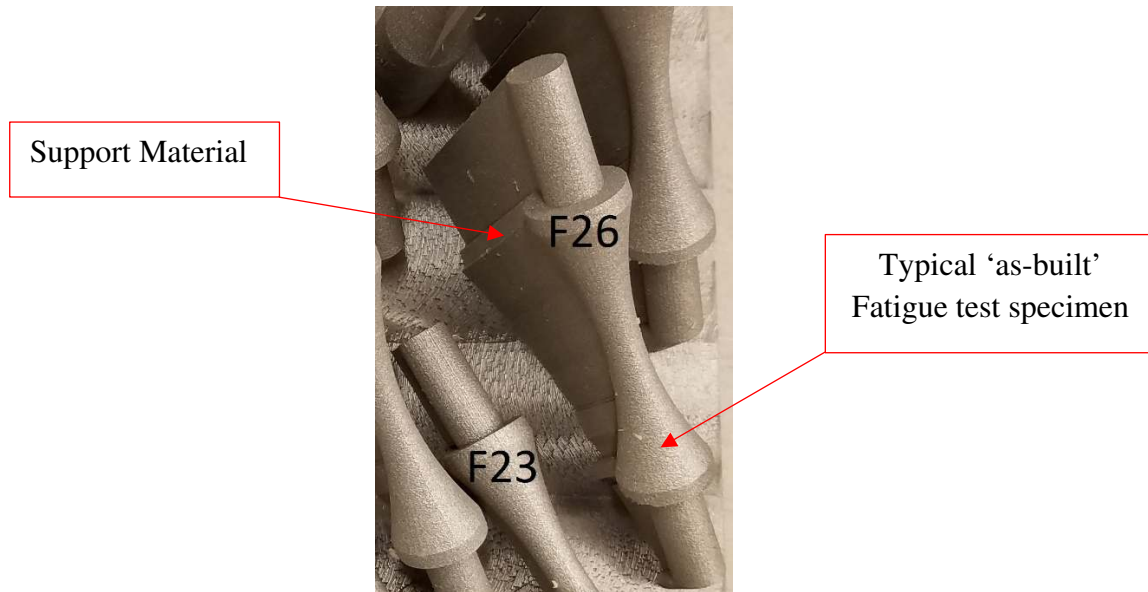


Figure 2: Image of Specimen on build plate. Arrow points to support structure.

1.2.2.1. Microstructures Observed

It has been observed that the microstructure of LPBF components are composed of fine segregated grains [5, 6, 9, 20]. The conditions used for LPBF printing using 316L stainless steel powder produces a specific and consistent microstructural development. Orientation of the component during construction has been observed to have a minimal effect on grain size [22]. Epitaxial grain growth across several melt tracks due to partial remelting with the deposition of subsequent tracks has been observed [24]. Direction of grain growth follows the maximum heat flux, in SLM this is the direction of laser travel, with deviation from ideal based on preferred growth direction from existing grains [4, 9, 23].

Solidification produces an austenitic microstructure with minute amounts of retained δ -ferrite distributed throughout the microstructure [3]. Under proper conditions, planar growth has been observed to occur at the base of melt tracks due to the inability to develop constitutional super cooling. When constitutional super cooling begins, due to a lower heat gradient, the

formation of cellular dendritic grains occurs. The high cooling rate typical with LPBF prevents the formation of secondary dendrites. Although the grains are cellular dendritic, the orientation from which they are viewed will affect the appearance. Viewing the long axis of the dendrites, their columnar appearance can be observed. Viewing the end fiber, the grains have an equiaxed cellular appearance [5, 9, 10, 23]. Marangoni flow, in conjunction with complicated heating and cooling cycles, causes the grains to grow in a variety of orientations even within the same melt track [3, 9]. If hot isostatic pressing (HIP) is employed in post processing, internal porosity can be reduced. This aids in the establishment of an intragranular cellular structure with nano-inclusions of oxides [7].

1.2.3. Mechanical Properties

Anisotropy, defined as a difference in properties along different axis, is a trait universal to AM components due to their layerwise construction [5, 6]. Selection of an appropriate scanning regime aids in minimizing anisotropic behavior [27]. By optimizing layerwise construction and anisotropic behavior in certain orientations, which can then achieve comparable or better properties than what is typically possible with traditionally crafted components [24].

Grain size is generally agreed upon as being the primary reason for improved strength for SLM components [9, 20, 24]. Strength is further improved by having fine distributions of δ -ferrite [3] and oxide nano-inclusions [7]. The fine grain size of AM components often leads to a higher component hardness than traditionally crafted counterparts [5]. The presence of a high volume of defects, which is common to AM, substantially reduces the benefit of the enhanced mechanical properties provided from a fine grain size [9, 21]. Residual stress from fabrication can result in subsequent hot or cold cracking [5], thus reducing the potential optimum capabilities of components.

Numerous LPBF studies have had contradictory results on the mechanical properties. This can partially be explained by differences in the process conditions under which specimens were constructed. Static tensile properties of LPBF 316L stainless have been observed in some studies to possess an improved yield strength and reduced UTS compared to wrought materials [1, 22], while others [9] report opposite findings in regard to yield strength and UTS. Some studies have indicated that orientation has minimal effect on tensile properties [20]. Other studies have indicated a substantial reduction for specimens constructed transverse to the build plate due to delamination of build layers [9, 22].

In general, LPBF components have been observed to possess a lower fatigue limit than that of their wrought counter parts [6, 20] This is especially true for those fabricated in the transverse orientation to the build plate [6, 20, 22, 28]. Reduction of fatigue limit for specimens constructed transverse to the build plate is theorized to be due to delamination between melt track layers [20, 22]. Specimens constructed longitudinal to the build plate have been observed to have an improved fatigue limit [22, 28]. Due to fatigue limit's dependency on surface quality and internal defect volume [29, 30], utilizing HIP has been observed to improve fatigue characteristics by reducing the internal void space and improve surface quality [20].

1.3. Notable Factors Effecting SLM

Research indicates there may be more than 130 individual factors affecting the properties of components built via SLM [31]. Given the number of factors that affect AM, only a few of the most cited will be discussed here. These factors include: key issues with powder properties, energy density during printing, atmospheric conditions, and some of the most commonly observed defects. Post processing is a common step that is often necessary and can greatly affect component behavior. The mechanical properties of components are affected by all of these

factors significantly requiring that they be accounted for. Little deviation from optimum conditions is required to lead to the development defects substantially reducing the quality of LPBF components.

1.3.1. Powder Properties

LPBF processes typically utilize powders that range from 10 to 130 μm and possess a wide variety of size distributions [2]. Powders produced via gas atomization with size distributions between 40 and 80 μm have had the best performance with existing technology [4]. Gas atomized powders are usually selected for SLM since they produce a tighter size distribution, lower oxygen content, and more spherical particle compared to water atomized powders [15].

When selecting a powder product for AM, it is important to consider the spreading mechanism. Compactness and size distribution of the powder have a strong effect on the flowability affecting the consistency of bed thickness, packing density, and composition. Powder flowability and packing efficiency are inversely related to each other. Non-uniform powder beds tend to leave void spaces and/or pockets of unmelted powder in final components [2]. Spherical powders are preferable for their consistent beam interaction and packing efficiency. Size distribution is critical to powder behavior during bed formation and lasing, too tight of a size distribution leads to poor packing efficiency and too broad leads to poor powder flow behavior [15, 32].

To improve the efficiency of heat transfer from the beam to the powder, surface modifications, such as roughening or oxidation, can reduce the coefficient of reflection [23]. If particle interaction after surface modification is not accounted for, then inconsistent rheological response can lead to non-uniform bed deposition [4]. Intentional surface oxidation should be

minimal since an oxide film as thin as a tenth millimeter can be sufficient to cause excessive heat buildup prior to the oxide layer freeing the trapped liquid [2]. Oxide layers on the powder reduce the amount of usable material and introduces oxide films to the melt negatively impacting strength.

Unmelted powder from printing can be recycled for reuse as a substitute for virgin powder. Experimentation indicates recycled powders have a slight improvement in flowability, reduced packing density, and slight increase in oxygen content [33]. Components constructed using recycled powders tend to have a reduced ductility and impact strength.

1.3.2. Energy Density

Energy density is a measure of heat input over unit area or volume and is derived from equations that have been historically developed for welding. Equation 1 is a common method of calculating volumetric energy density. The equation can be used for calculating area energy density if the term for bed depth (t) is removed. Determining the optimum energy density is difficult due to it being a composite value derived from factors that both dependently and independently affect the microstructure, and therefore mechanical properties of AM components. Studies using stainless steel powders have required energy densities ranging from 89 J/mm^3 [24] to more than 125 J/mm^3 [9] to achieve full densification. A medium value of approximately 104 J/mm^3 has been cited in several sources as an optimum energy density for 316L stainless steel [3, 10].

Equation 1: Formula for the calculation of volumetric energy density.

$$E = \frac{P}{v * h * t}$$

Volumetric energy density (E) in J/mm³, laser power (P) in watts, laser scan speed (v) in mm/s, hatch spacing (h) in mm, and layer thickness (t) in mm [5, 24].

Achieving an appropriate energy density is critical to producing a serviceable component. Insufficient energy density produces inconsistent melt tracks with poor stability, a propensity for lack of fusion defects, and poor interlayer fusion. As the energy density is increased from the optimum value, melt tracks will widen and have an extended solidification period [24, 27]. It is indicated that increasing the energy density is beneficial until reaching a critical point at which the excess energy begins to promote balling, spattering, and residual stress therefore weakening the component [5]. Excessive energy density causes alloy vaporization leading to vapor recoil pressure sufficient to cause a transition to keyhole-mode melting. Penetration is greatly increased but leads to the development of unstable melt tracks and increased residual porosity when operating in keyhole-mode melting [34].

It is theorized heat input is the most important factor in achieving fully dense components. A high laser power allows a broader range of scan speeds, and by extension heat inputs, to achieve full densification [11]. Since densification is usually the chief concern with AM components, heat input can often be used as the initial term for determining an optimum energy density. Preheating the build chamber prior to lasing can be treated as an additional heat input to the system and may allow for a reduced heat input from the laser. Preheating has the effect of adjusting the wettability and increasing melt track penetration; however, if it exceeds half of the melting temperature, the melt track stability is reduced promoting balling and spattering [16].

Balancing the scan speed and the hatch spacing is important when developing an optimum energy density. Cracking across the width of the melt track occurs with too great of a hatch spacing. Large hatch spacing requires a slower scan speed which increases the heat input required for proper pool formation. There are two theories for crack development across the melt track. The first is that the low scan speed allows for a greater heat buildup between hatches lowering the cooling rate leading to film formation between grains. The brittle film between the grains cannot sustain the stress of shrinkage as the area cools. The second theory is that increased heat input to local areas can cause a transition to keyhole-mode melting whose residual porosity promotes cracking [3]. By employing a scan strategy that utilizes short scan vectors and a varying scan direction, the residual stress in the component can be reduced and will be more evenly distributed [35] which will further reducing the likelihood of cracking. Besides preventing cracking across the melt track, this tighter hatch spacing can improve the surface finish of components [10].

1.3.3. Atmosphere

The atmospheric conditions under which the powder is stored and components constructed can greatly affect how the powder will behave. Most metallic powders will readily form an oxide in the presence of air. Oxidation of the metal powders causes issues during component construction including the introduction of brittle oxides to the melt and reduction of melt track stability. Apart from surface oxidation, water infiltration is the other major concern for powder contamination. The high energy input in SLM is sufficient to dissociate trapped moisture. Entrapped hydrogen can cause metal hydrides or hydroxides which are highly deleterious to the strength of the component [2].

The atmosphere inside the build chamber needs to be carefully controlled to prevent plasma formation from scattering the laser beam reducing heat input [23]. Pressure within the build chamber has the dual effect of aiding in control of melt track stability and denudation of the powder bed. Insufficient chamber pressure decreases the volatilization temperature which can promote keyhole-mode melting. Denudation can occur if there is sufficient vapor recoil pressure to blow powder away from the advancing melt track's front and sides [18]

1.3.4. Commonly Observed LPBF Defects

Dimensionality and mechanical properties are the primary categories that defects affect. Surface quality, a measure of dimensionality, can affect the mechanical response of components as they act as stress raisers [36]. Defects observed in LPBF often manifest as internal void spacing. Void spacing most often arises from a combination of balling, spattering, lack of fusion, and trapped gas porosity. It is theorized that manufacturing defects are primarily controlled by the amount of heat in the melt [19].

When the temperature of the melt track is approaching the liquidus, there is insufficient heat to form a stable melt track. Insufficient heat manifests as ropey melt tracks leading to a reduction in surface quality and poor melt track fusion [10]. Too low of a heat input will prevent achieving the penetration necessary for good fusion between build layers [37]. As the temperature increases away from the liquidus until it approaches the boiling point, Marangoni force controls flow dynamics within the melt track. In this temperature range, melt track stability is largely determined by surface tension and wettability; a low wettability promotes balling, and a negative surface tension promotes poor penetration. Balling and spattering will increase in frequency and volume as the temperature approaches the boiling point [16]. Evaporative cooling controls flow mechanics in the melt once the boiling point has been reached. Keyhole-mode

melting will take over above the boiling point leaving a greater volume of defects. Surface quality will decrease while operating in keyhole-mode melting and increase balling, spattering, and residual porosity [19].

Balling is among the most commonly observed defects in SLM [4, 9, 10] and is one of the most detrimental defects for surface quality in LPBF. Balling arises from capillary instability related to the wettability of the melt track to the powder and the convective forces at play from surface tension; both can be treated as functions of temperature. When the wettability is insufficient to prevent surface tension of the material from drawing into a sphere to reduce the surface energy balling occurs. It is observed in higher frequency when the energy density strays too far from optimum. Too low of an energy density will develop many small balls. Too great an energy density, the volume of balls developed will increase and form in a variety of sizes [10]. When using stainless steel powder, it is impossible to avoid some balling due to the reactivity of iron and chromium with oxygen which increases surface tension [5].

Denudation arises from powder loss in areas of the powder bed. Experimentation has indicated that denudation primarily occurs from the Bernoulli effect pulling powder into the melt track [14, 21]. The Bernoulli effect is induced from vaporization of metal in the melt track. Further, as previously discussed, excessive gas evolution can blow powder away from the advancing melt track. Another source of denudation comes from excessive surface roughness resulting from melt track instability preventing a uniform deposition of powder on the subsequent pass [27]. Denudation of powder can have a strong negative impact on the surface quality of the component [14], and in extreme cases, lead to regions of poor fusion with subsequent layers or adjacent melt tracks.

Porosity, either as gas entrapment or lack of fusion voids, is the most commonly observed defect in AM [4, 6, 20]. Porosity can arise from any of the above defects discussed. Deviation from an optimum energy density will increase internal porosity [10, 11]. Porosity generally has a negative impact on mechanical properties. The distribution and morphology of defects can have a significant impact on the extent of degradation [13, 38]. Sub-micron porosity, resulting from solidification shrinkage, is prevalent in AM components; HIP has been found to effectively reduce this form of porosity [4].

There is a tendency for powder particles to partially fuse to the outer surface of the component during SLM which contributes to a poor surface quality. Variations in geometry have been found to promote partial fusion of powder particles due to a concentration of melt tracks in a smaller area [39].

1.3.5. Post Processing Techniques

It is common for some degree of post processing to be required. The most basic task is the separation of components from the build plate and excess powder removed. It may be necessary to undergo heat treatment to modify the microstructure to the desired state or relieve stress. HIP is a popular heat treatment for AM components to reduce internal porosity improving mechanical performance [4, 20]. Although a popular option, mechanical polishing has been shown to be only partially useful in improving surface quality of components as it exposes internal defects [20]. Laser remelting extends production time but can remove the need for secondary processing, such as HIP, to increase final component density. Another benefit to laser remelting is that it can be utilized to improve the dimensionality of components [12].

2. RESEARCH OBJECTIVES

Mechanical testing and material analysis were performed to evaluate the mechanical and material properties of LPBF processed 316L stainless steel by:

1. Evaluating the ultimate tensile stress,
2. Surveying the fatigue limit,
3. Characterizing the failure mode for tensile and high cycle fatigue fracture specimens,
4. And examining the microstructure for apparent melt track and dendrite size.

3. METHODOLOGY

3.1. Material and Specimen Creation

Using 316L stainless steel powder with the composition outlined in Table II, LPBF test specimens were printed. Specimens were made using an EOS M290 printer by a third-party vendor.



Figure 3: Image of an EOS M29 Printer [41]

Table II: Chemical composition of stainless steel powder used for construction of AM components.

Element	Wt. %
Cr	16.94
Ni	12.09
Mo	2.38
C	0.009
Si	0.48
Mn	1.20
P	< 0.005
S	0.005
N	0.01
Total Other	0.1
Fe	Balance

Specimens were printed with an energy densities of either 55.6 J/mm^3 , 100.0 J/mm^3 , or 187.6 J/mm^3 . Table III details the specific process parameters used for each set of specimens. For each energy density, specimens were constructed at various orientations to the build plate. Specifically, specimens were constructed at 0° (longitudinal), 45° , and 90° (transverse) orientations for this study. All specimens were freed from the 316L stainless steel build plate and lathed to final dimension to minimize surface roughness. No specimens were tested in an ‘as-built’ condition from the printer.

Table III: Process variables and energy densities for the sets of test specimens constructed.

Build Set	Laser Power (W)	Scan Speed (mm/s)	Hatch Spacing (mm)	Layer Thickness (mm)	Energy Density area (J/mm^2)	Energy Density volume (J/mm^3)
Low Energy Density	156	1300	0.11	0.02	1.1	55.6
Medium Energy Density	195	1083	0.09	0.02	2.0	100.0
High Energy Density	234	866	0.07	0.02	3.8	187.6

3.2. Tensile Testing

Tensile testing was performed using an MTS Landmark Servo-Hydraulic Test Frame following ASTM E8 standard for testing. Each combination of build set and orientation were tested in triplicate to form an average. For this study, the UTS was the value of interest.

3.3. Fatigue Testing

Fully reversed high cycle fatigue testing was performed on a Fatigue Dynamic’s Inc. RBF-200. The moment was determined by using Equation 2. The stress was determined by using a percentage of the UTS; for this study, specimens were tested at 55%, 60%, and 65% of the UTS. Ten million (10^7) cycles were taken as the infinite fatigue limit.

Equation 2: Formula for the calculation moment for fatigue testing using a Fatigue Dynamics Inc. RBF-200. [42]

$$M = \frac{\pi * s * d^3}{32} = 0.0982 * s * d^3$$

Momentum (M) in in-lb, stress (s) in psi, and diameter (d) in inches.

3.4. Fractography

Representative tensile and fatigue specimens were selected after fracture for examination. The selected specimens had the fracture surface cut away from the component body for analysis using a slow cut saw. The freed fracture surface was then washed with reagent alcohol using an ultrasonic sonication bath. The washed specimens were then examined, and images collected using a LEO 1430VP scanning electron microscope operated in secondary electron detection mode.

3.5. Microstructural Analysis

After mechanical testing, representative specimens were selected for microstructural analysis. The selected specimens had their grips sectioned using a slow cut saw to generate an 'XY' and a 'Z' sample. The XY samples were for examining the surface perpendicular to the long axis of the specimen and the Z to examine the parallel, depicted Figure 4. Polished specimens were etched using Vilella's reagent. Etched specimens were imaged using a Leica DM750P at 100X and 1000X. The samples were imaged ten times at random locations for each magnification. Images were analyzed using the Leica Application Suite V4.8 grain expert feature. The 100X images were used for measuring the apparent melt track area, length, and breadth. Apparent melt track size in this study is taken as the area, length, and breadth of a melt track that is observable on the etched specimen. 1000X images were used for analyzing the area,

length, and breadth of the dendrites. The grain expert measurement results for the ten images were collated together for statistical analysis.

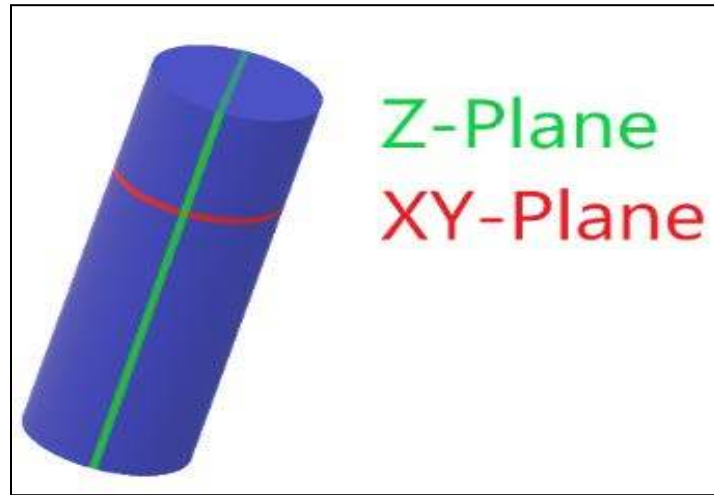


Figure 4: 'XY' and 'Z' sample orientations

4. RESULTS

4.1. Ultimate Tensile Strength

The average UTS was established for each build set and orientation tested for this study presented in Figure 5. The longitudinal and 45° orientations were relatively consistent across all the energy densities having a maximum difference of 4% between the longitudinal and 45° orientation medium energy density specimens. Transverse orientation specimens possessed a much greater variation in UTS between energy densities. The greatest difference in transverse UTS was 24% between the low and medium energy density. In general, the longitudinal specimens had a marginally improved UTS over the 45° orientation specimens and even more so than the transverse orientation. The exception to this was the medium energy density specimens constructed transverse to the build plate which had the greatest average UTS in the study. The coefficient of variation was less than 5% for any given set of tensile specimens tested; see Appendix A Table IV for tabulated results.

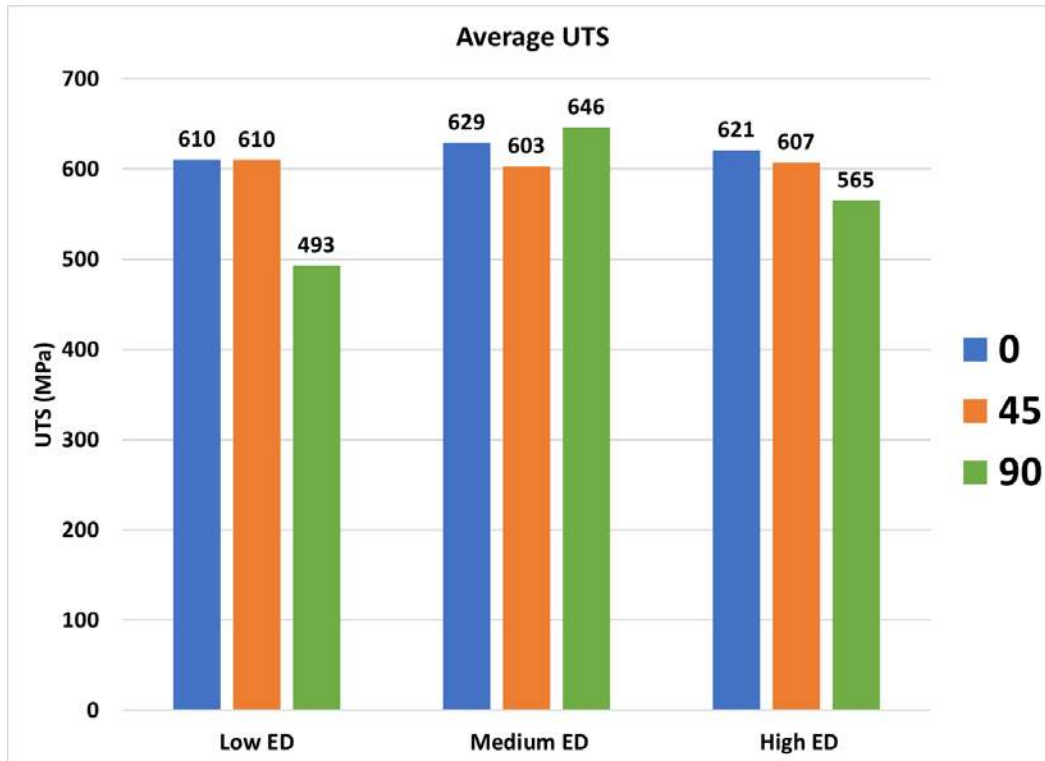


Figure 5: Average UTS of specimens studied.

4.2. High Cycle Fatigue

The low energy density set, Figure 6, possessed a generally low fatigue limit. The fatigue limit varied significantly depending on the orientation. The longitudinal and transverse orientations followed the normal trend of a reduction in fatigue limit as the stress increased. The 45° orientation test specimens had a slight increase in fatigue limit for the 60% UTS loading as compared the 55% UTS loading. The transverse orientation possessed the highest fatigue limit of the low energy density set. The only specimen to achieve ten million cycles for the low energy density set was at 55% of the UTS in the transverse orientation.

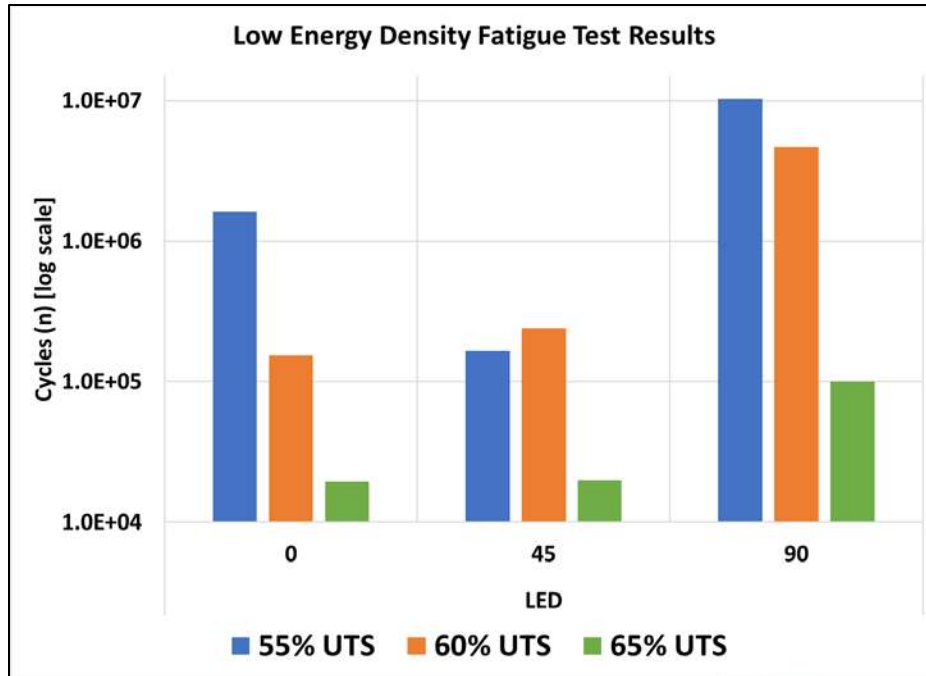


Figure 6: Low Energy Density (55.6J/mm³) Fatigue Test Results

The medium energy density set, Figure 7, had the greatest highest limit of the energy densities tested. The longitudinal orientation had the lowest fatigue limit of the set with only the 55% UTS loading achieving ten million cycles. Fatigue limit for the longitudinal orientation followed the standard inverse relationship of stress with fatigue limit. The 45° orientation specimens all achieved ten million cycles. The transverse orientation specimens achieved ten million cycles at 55% and 60% of the UTS. The 65% of UTS loading for the transverse orientation had a substantial reduction in fatigue limit fracturing at approximately eighteen thousand (1.8×10^4) cycles; the lowest fatigue limit in this study. See Appendix A Table V for tabulated fatigue test results.

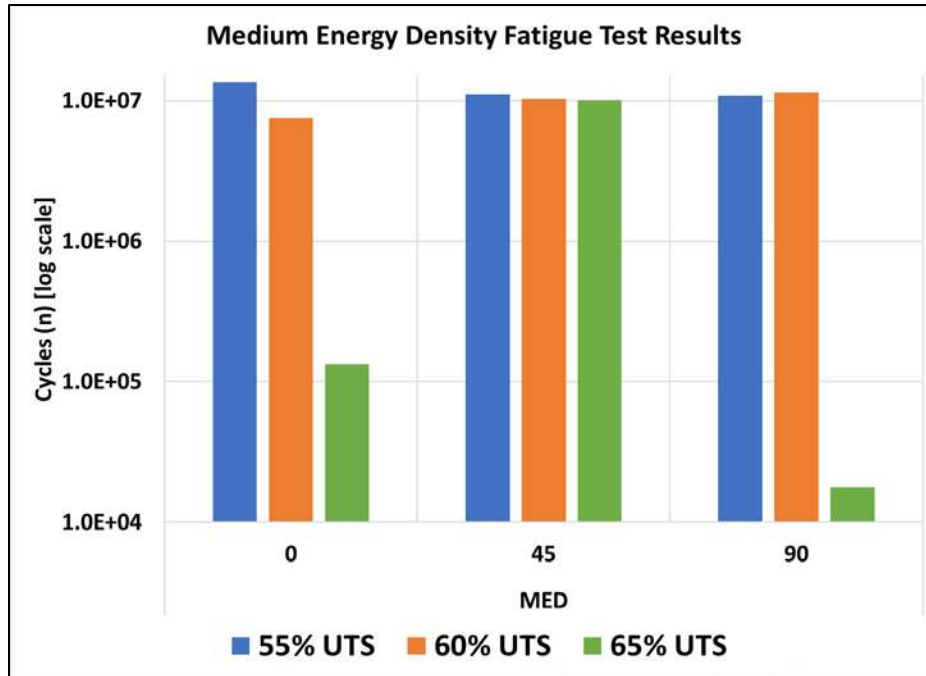


Figure 7: Medium Energy Density (100.0 J/mm³) Fatigue Test Results

The high energy density set, Figure 8, had a low fatigue limit with only the 55% of UTS specimens achieving ten million cycles. The greatest fatigue limit for the high energy density set was the longitudinal orientation. At 60% of UTS the longitudinal orientation had approximately twice the cycles to fracture over the 45° and transverse orientation specimens. The high energy density set had the most consistent fatigue limit tested in the study.

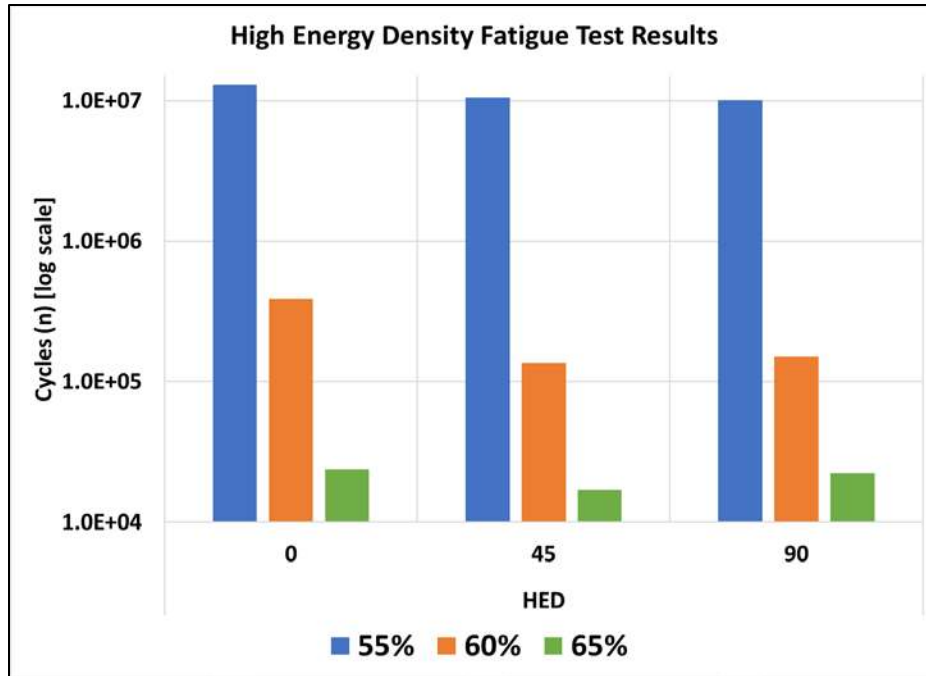


Figure 8: High Energy Density (187.6 J/mm³) Fatigue Test Results

4.3. Fractography

The tensile specimens observed for fractography all fractured in a predominantly ductile mode. Specimens fractured with a mix of moderate ductility, low ductility, and brittle features. Most specimens fractured with a classic cup-and-cone macro surface expected of moderate ductility material. Though still ductile, some specimens fractured with an approximately flat macro surface perpendicular to the axis of loading. See Appendix B for example diagram of tensile specimen with call outs for ‘cup’ side, ‘cone’ side, and ‘shear lip’ for a moderate ductility fracture surface.

Crack initiation for the fatigue specimens arose from defects at the specimen surface. The crack propagation zone could typically be identified by the presence of striations. Many of the specimens examined fractured with relatively few cycles which contributed to the generally

small crack propagation zones. The final fracture zone could typically be identified by a transition to a flat planar fracture surface.

4.3.1. Low Energy Density Tensile Fractography

The low energy density tensile specimens examined fractured predominantly in a ductile mode. As observable in Figure 9, the low energy density specimens had a rough, approximately flat fracture surface perpendicular to the axis of loading. Plastic flow, a characteristic of ductile mode fracture, is indicated by the presence of relatively smooth contours. The longitudinal and 45° orientation specimens were similar except that the 45° orientation was observed to have a greater volume of defects.

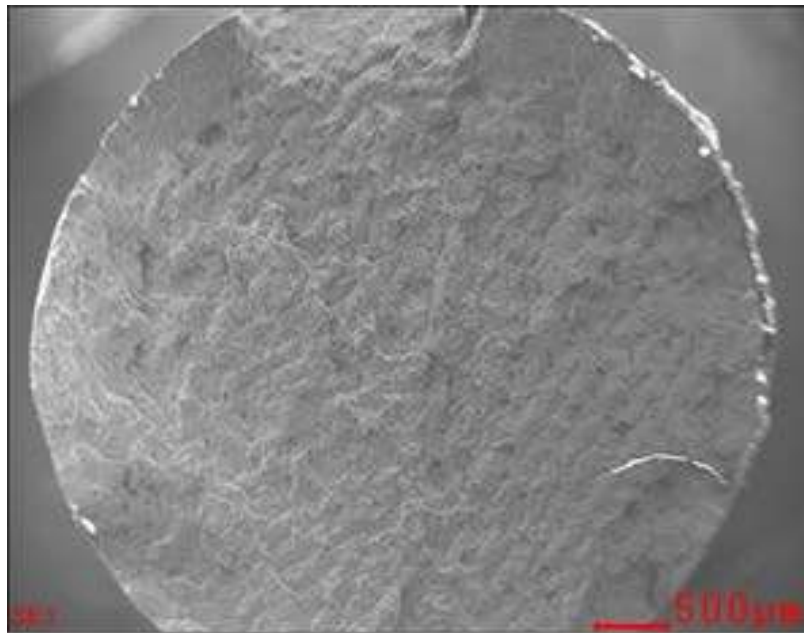


Figure 9: 55.6 J/mm³ energy density 0° orientation tensile fracture surface. Predominantly ductile failure mode with a flat fracture surface

The specimens examined for the low energy density had a mixture of moderate to low ductility features. Moderate ductility regions were indicated by the presence of dimpling and fine ductile pores as observed in Figure 10's boxed area A. Low ductility regions had little to none of the

fine dimpling or ductile pores as encircled in area B of Figure 10. Moderate sized shallow voids were distributed across the specimen surface; an example is indicated by the C arrow in Figure 10.

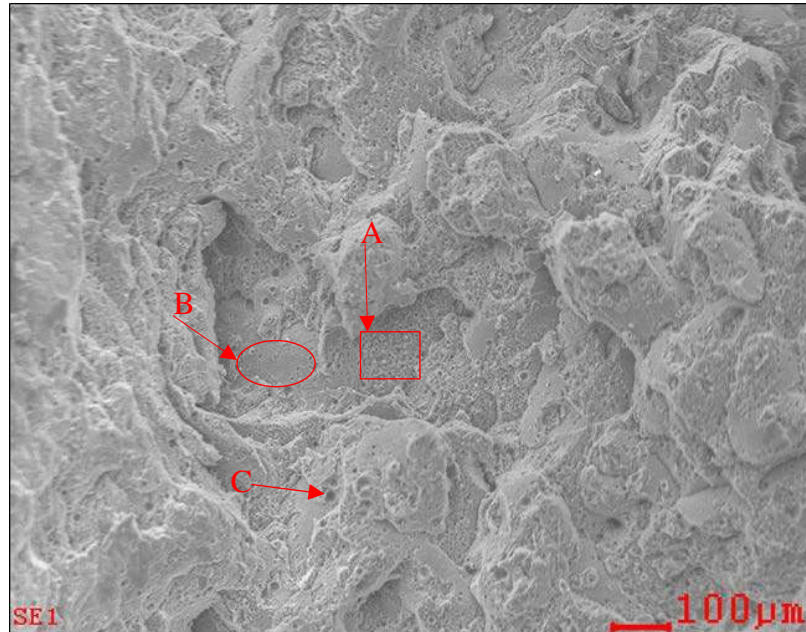


Figure 10: 55.6 J/mm³ energy density 0° orientation tensile fracture surface. Fracture surface is mix of high ductility and moderate ductility features. Moderate ductility material is determined by the presence of dimpling and fine spherical porosity; see region A. Areas lacking fine dimpling but still with indication of plastic flow are a low ductility; see region B. Arrow C points to a moderate sized shallow void.

Regions of brittle features were observed across the fracture surfaces of the low energy density tensile specimens. An example of several types of brittle features and defects are shown in Figure 11. Frame 1 is of a brittle region with angular features protruding from the specimen surface. Angular voids with brittle features shown in Frame 2 were observed in a relatively high volume across the surface of the 45° orientation specimen. Angular voids frequently had secondary cracking and sharp angular features on and around them. Two different types of lack of fusion defects were observed on longitudinal and 45° orientation specimens. The first type was partial fusion of powder particles with ductile features as shown in Frame 2 pointed to by B.

The second type of lack of fusion defect was clumps of partially fused powder particles covered in brittle features; an example is presented in Frame 3.

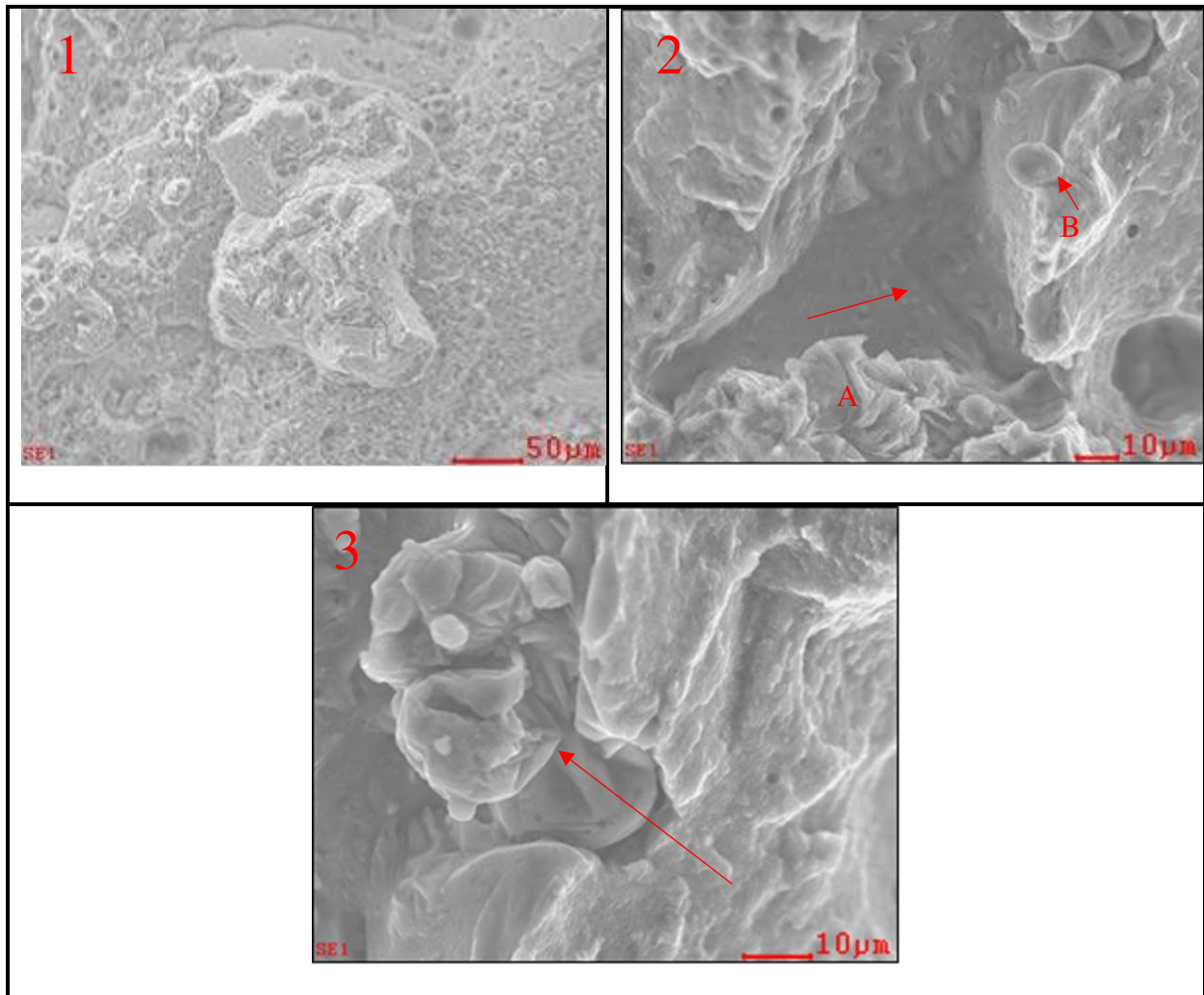


Figure 11: 55.6 J/mm³ energy density at the 0° for Frame 1, and 45°, Frames 2 and 3, tensile fracture surfaces. Frame 1: Example of brittle features distributed across the failure surface and are identified by angular fracture surfaces. Frame 2: Angular void with brittle features such as secondary cracking (arrow indicates) and angular surfaces, A. To right of void is a partially fused powder particle, B, in a region of moderate ductility. Frame 3: Clump of partially fused powder particles with brittle features, arrow indicates.

The low energy density transverse specimen examined, apart from possessing a flat fracture surface, had a fracture surface that was dissimilar to the longitudinal and 45° orientations. The fracture surface was composed of partially fused melt tracks as shown in Figure 12. Fracture occurred between layers of melt tracks with an occasional step to a different layer.

The well preserved surface of the melt tracks indicate that there was little fusion between layers across the majority of the fracture surface.

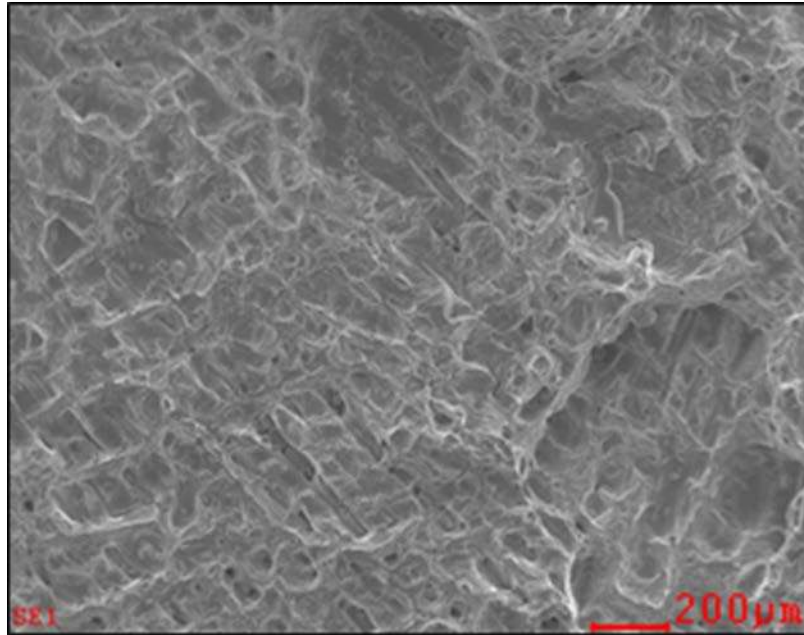


Figure 12: 55.6 J/mm³ energy density 90° orientation tensile fracture. Fracture surface that broke between layers of melt tracks. Individual melt tracks are identifiable and poorly fused to each other.

There were many partially fused powder particles between the melt tracks and to a lesser extent on the top of the melt tracks as displayed in Figure 13. Faint depressions on the melt tracks indicate where powder particles either didn't fuse or just slightly fused to the surface and fell away after fracture occurred. Areas of plastic deformation with a rough texture indicate a low ductility failure mode in the regions of fusion. Regions with fusion predominantly had a high volume of voids with a mixture of circular and irregular, near oval, shapes.

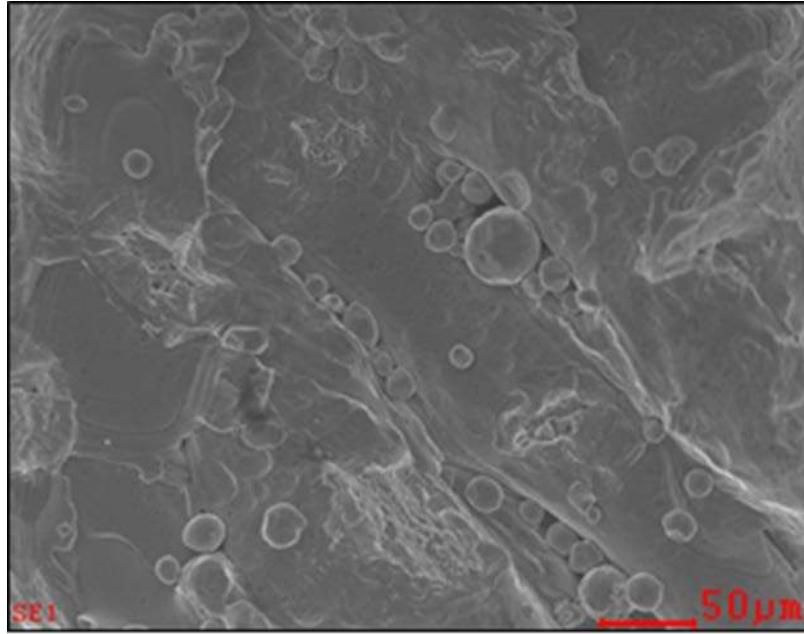


Figure 13: 55.6 J/mm³ energy density 90° orientation tensile fracture. Poorly fused melt tracks and powder particles.

4.3.2. Medium Energy Density Tensile Fractography

The medium energy density tensile specimens examined fractured with a predominantly ductile failure mode. The longitudinal specimen fractured with a ductility sufficient to develop shear lips. Ductile tearing along the base of the shear lip and across the central region of the fracture surface, shown in Figure 14, supporting ductile mode fracture. The fracture surface in the central region had a honey comb structure, as observed in Figure 15, further indicating ductile mode fracturing. Large irregular shaped voids were distributed across the fracture surface in a moderate volume with the majority being in the central region.

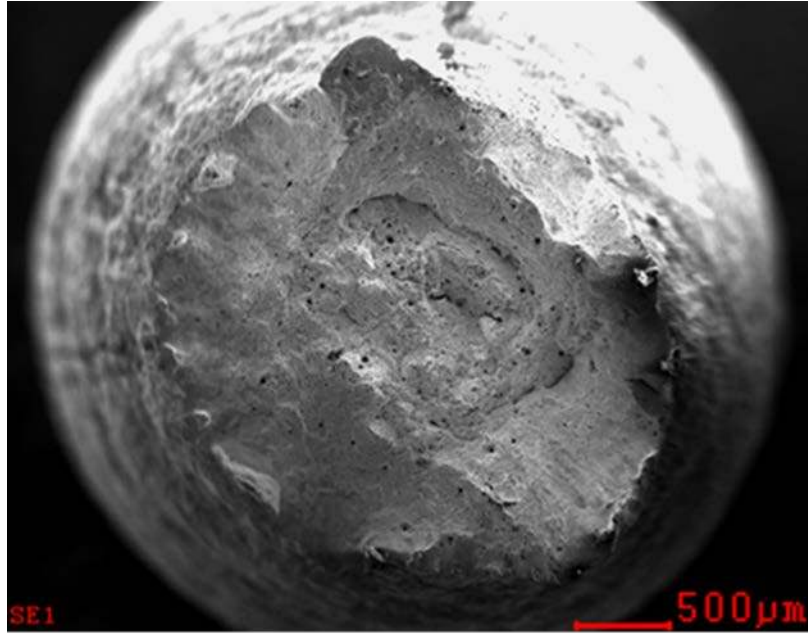


Figure 14: 100.0 J/mm³ energy density 0° orientation tensile fracture. Ductile failure mode with well-developed shear lips. Ductile tearing at the base of the shear lips and central area of fracture surface. Moderate distribution of irregular pores across the fracture surface.

At higher magnification, the irregular shaped voids were observed to possess ribbing that traversed the interior and along the entire length of the defect. At the base of irregular voids, when observable, lack of fusion defects were present. The ‘A’ arrows in Figure 15 point to two examples of lack of fusion defects at the base of irregular voids. At the edge of irregular shaped voids, there were small areas of brittle features; an example of one of the larger brittle areas is pointed to by the ‘B’ arrow in Figure 15. Smaller, irregular shaped voids were interspersed around the large voids.

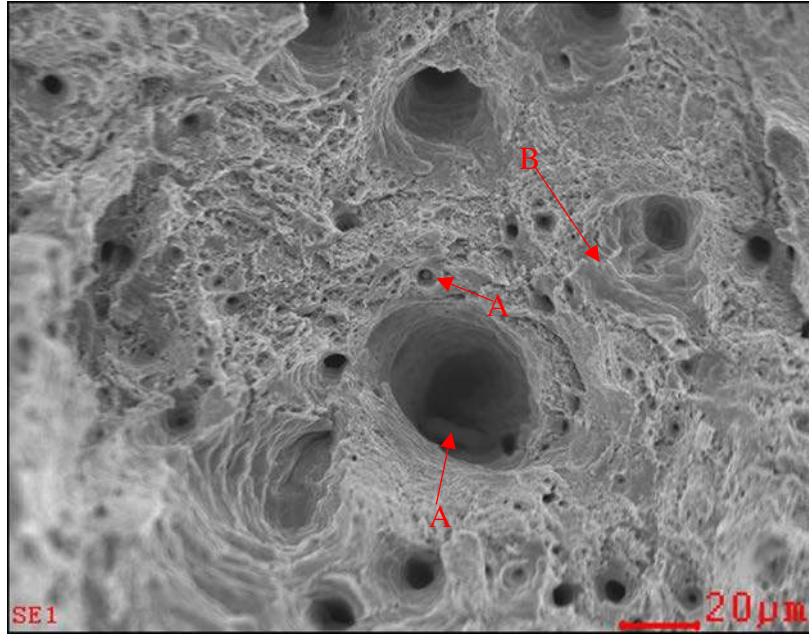


Figure 15: 100.0 J/mm³ energy density 0° orientation tensile fracture. Honey comb structure with irregular voids observed to have lack of fusion defects (A arrows) at their base and ribbing that traversed the interior of the void the entire length. B arrow points to area of brittle features

The 45° orientation specimen examined possessed a fracture surface that differed significantly from the longitudinal and transverse medium energy density specimens. The specimen fractured with a relatively flat fracture surface, shown in Figure 16, reminiscent of the low energy density specimens. The fracture surface is composed primarily of low ductility semi-smooth contoured surfaces. Brittle angular voids were distributed across the fracture surface. As shown in Figure 17 the voids were most often shallow and covered in brittle features, most predominantly sharp angled protrusions.

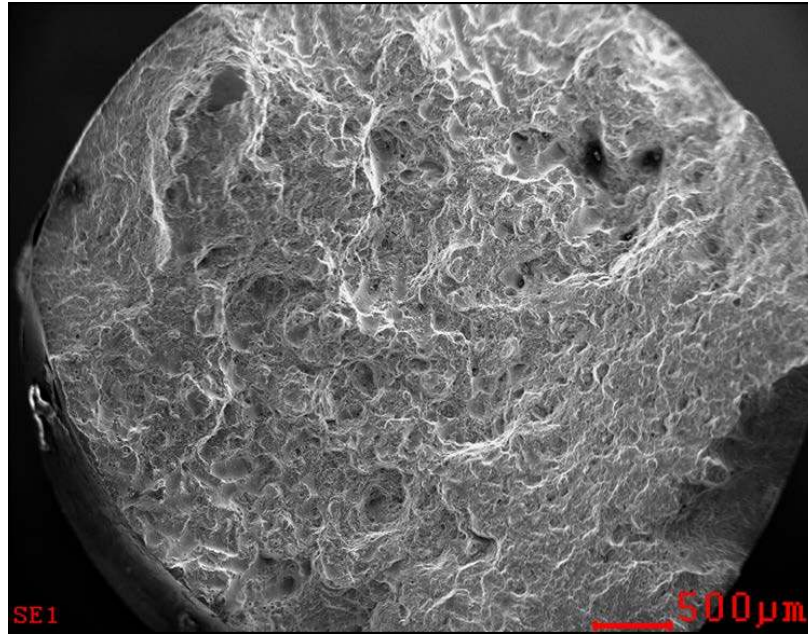


Figure 16: 100.0 J/mm³ energy density 0° orientation tensile fracture. Predominantly ductile failure mode with a flat fracture surface and high volume of voids.

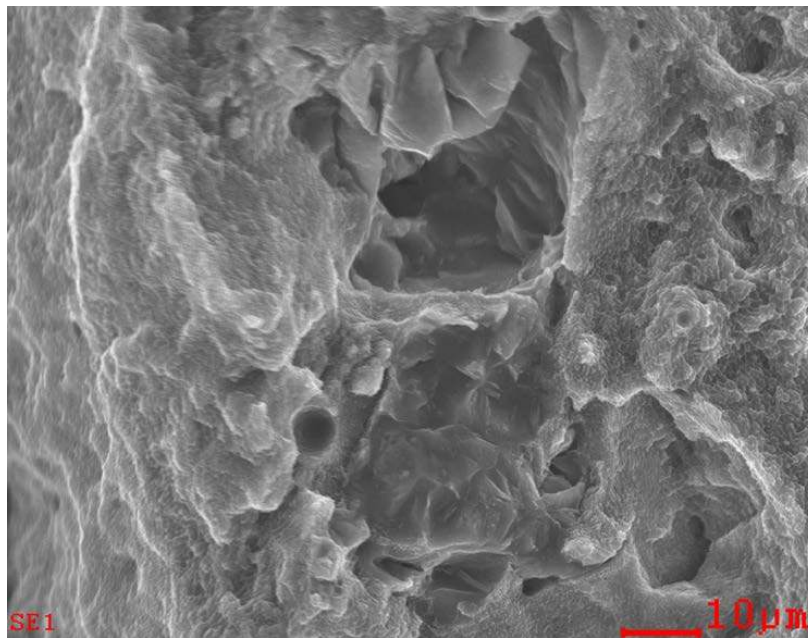


Figure 17: 100.0 J/mm³ energy density 45° orientation tensile fracture. Example of angular brittle voids observed distributed across the specimen surface.

The transverse specimen of the medium energy density set was similar to the longitudinal. The specimen fractured in a ductile mode with moderate ductility as indicated by its

development of shear lips and honey comb structure as shown in Figure 18. Ductile tearing was predominantly at the base of the shear lip. A moderate distribution of irregular shaped voids populated the central region of the fracture surface.

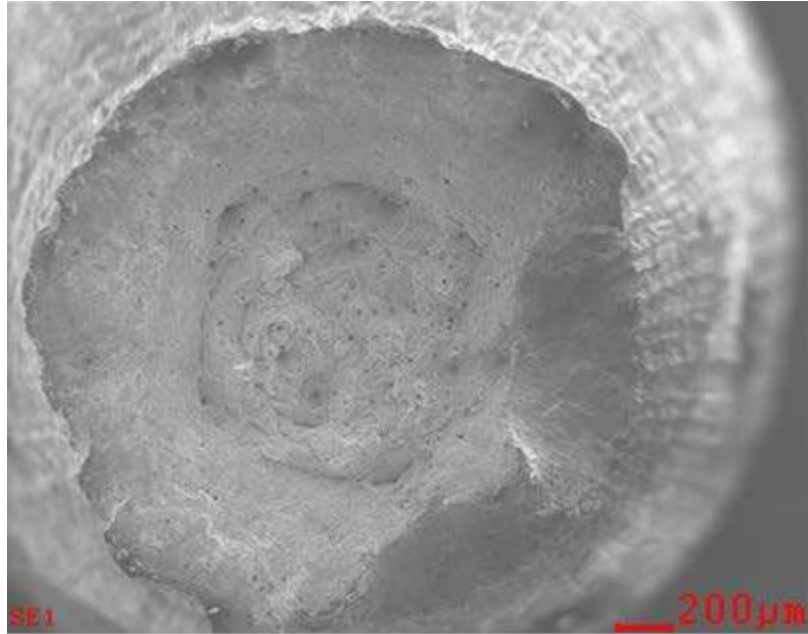


Figure 18: 100.0 J/mm³ energy density 90° orientation tensile fracture. Ductile failure mode with well-developed shear lips. Ductile tearing at the base of the shear lips and central area of fracture surface. Moderate distribution of irregular pores across the fracture surface.

4.3.3. High Energy Density Tensile Fractography

The high energy density specimens fractured in a ductile mode with well-developed shear lips and a honey comb structure, shown in Figure 19. The honey comb structure is more apparent at higher magnification, shown in Figure 20. Ductile tearing could be observed at the base of the shear lip and in the central area of the fracture surface. A small number of large irregular voids were distributed across the central area of the fracture surface.

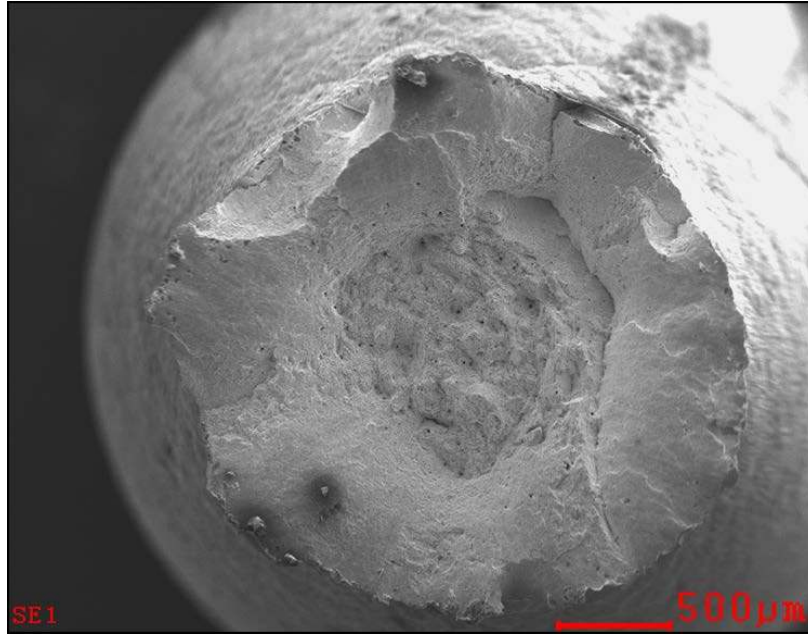


Figure 19: 187.6 J/mm³ energy density 0° orientation tensile fracture. Ductile failure mode with well-developed shear lips, ductile tears and low distribution of irregular voids.

The irregular shaped void presented in Figure 20 highlights the ribbing common to this type of defect observed with the medium and high energy density tensile fractography specimens. The interior surface of the void was observed to have secondary cracking that indicates it being a brittle material. The interior brittle rind was breaking away from the specimen at several locations. A smooth walled circular pore shown in Figure 21 indicates the presence of gas entrapment.

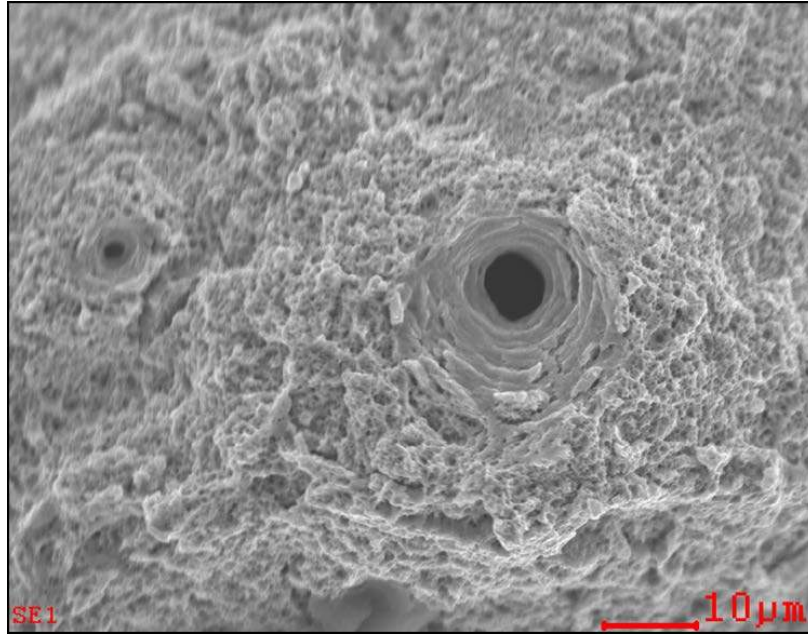


Figure 20: 187.6 J/mm³ energy density 45° orientation tensile fracture. Honey comb structure with an irregular void possessing a rind of brittle material.

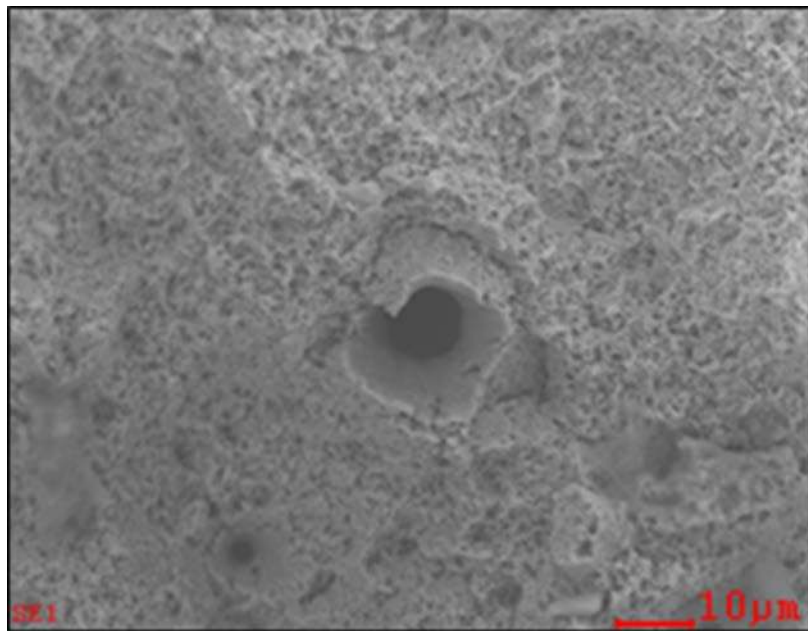


Figure 21: 187.6 J/mm³ energy density 90° orientation tensile fracture. Honey comb structure with a smooth walled circular void.

4.3.4. Low Energy Density Fatigue Fractography

Crack initiation for the low energy density longitudinal specimen arose from a pair of adjacent surface defects. Initiation site B fractured over to a large lack of fusion defect where the majority of crack propagation occurred. The crack propagation zone went into the specimen approximately 200 μm ; the end of the crack propagation zone is outlined in Figure 22. Specimen fractured with a 55% of UTS loading at 1.62×10^6 cycles.

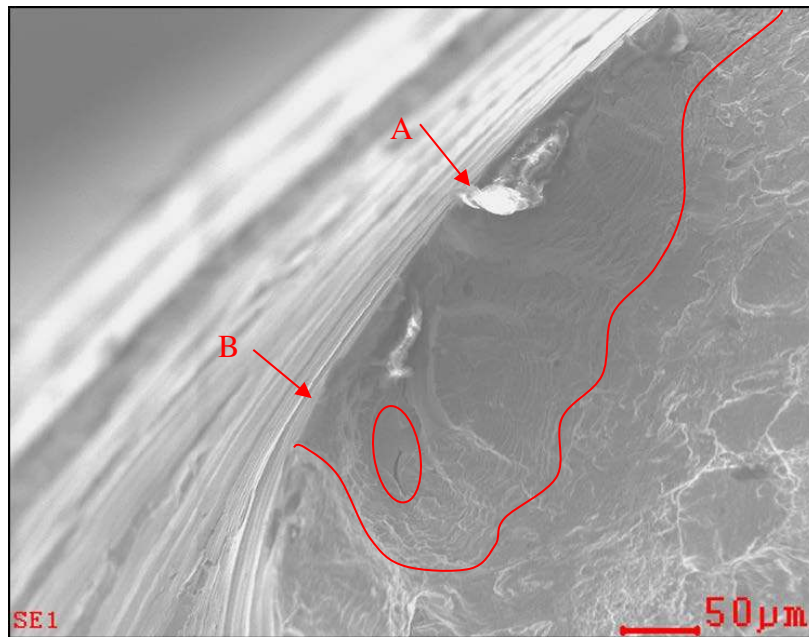


Figure 22: 55.6 J/mm³ energy density 0° orientation fatigue fracture. Red arrows point to pair of crack initiation sites. Enclosed is large lack of fusion defect where most of lower crack propagation occurred. Red line traces approximate end of crack propagation zone.

The fast fracture zone was brittle with angular features fracturing along cleavage planes. The final fracture zone is demarcated by a transition to a flat planar fracture surface as it approaches the opposite end of the specimen from the primary crack propagation zone. The fast fracture zone and final fracture zone shown in Figure 23 are typical to most of the specimens examined in this study.

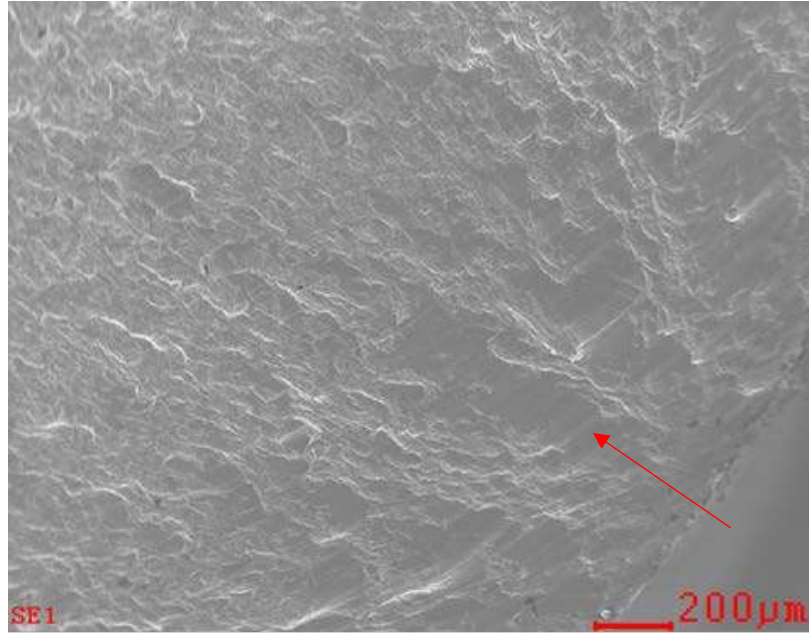


Figure 23: 55.6 J/mm³ energy density 0° orientation fatigue fracture. Brittle fast fracture and final fracture zone. Final fracture zone identifiable to flat planar fracture surface, red arrow indicates.

The low energy density 45° orientation specimen had crack initiation arise from a lack of fusion defect at the specimen edge, indicated by arrow in Figure 24. The crack propagation zone was small, only extending approximately 50 µm into the specimen. The fast fracture zone for this specimen with its large volume of voids differs from what was typically observed in this study. Specimen fractured with a 55% of UTS loading at 1.66×10^5 cycles.

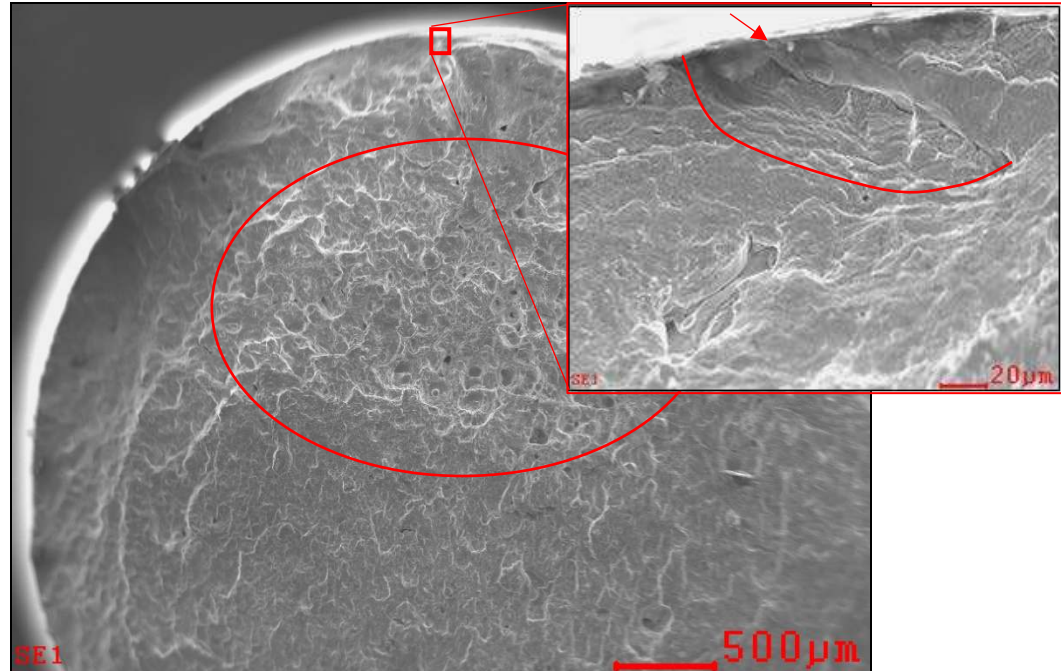


Figure 24: 55.6 J/mm³ energy density 45° orientation fatigue fracture. Red arrow in magnified image points to lack of fusion defect from which crack initiation occurred. The approximate transition point between the crack initiation zone and fast fracture zone is outlined in the magnified image. A high volume of irregular shaped voids is observed in the first third of fast fracture zone, enclosed in oval.

The transverse specimen for the low energy density had crack initiation from a surface defect which fractured over to a large lack of fusion defect. It is from the lack of fusion that primary crack propagation arose. Crack propagation for this specimen had no striations as typically observed but was identifiable by its smooth surface which transitioned to a typical brittle fast fracture zone. Figure 25 shows the crack initiation site, propagation zone, and beginning of the fast fracture zone. Specimen fractured with a 60% of UTS loading at 4.65×10^6 cycles.

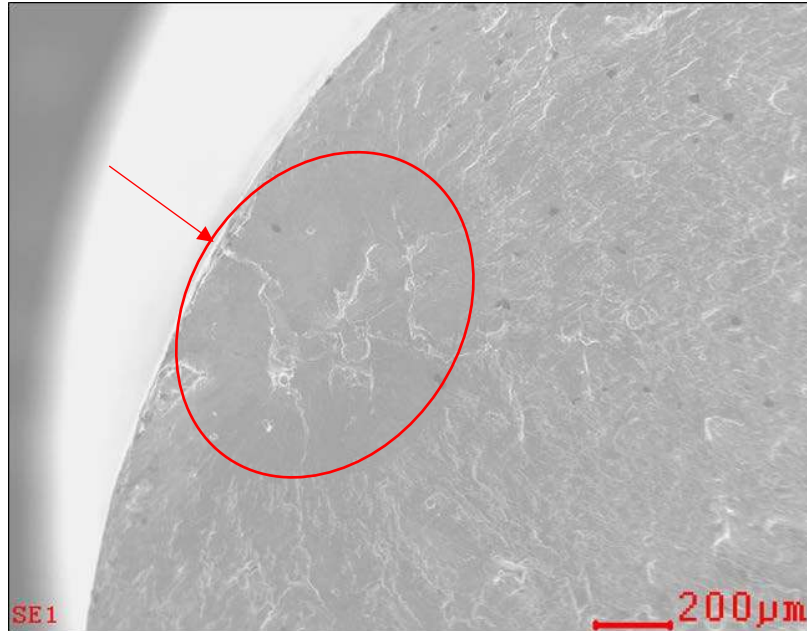


Figure 25: 55.6 J/mm³ energy density 90° orientation fatigue fracture. Red arrow points to crack initiation site, a small surface defect. Crack broke over to a large lack of fusion defect center of crack propagation zone, enclosed in oval.

4.3.5. Medium Energy Density Fatigue Fractography

The medium energy density longitudinal orientation specimen had the largest crack propagation zone observed in the study. Crack initiation arose from a surface defect. The propagation zone extended approximately a third of the way into the specimen. The central region of the crack propagation zone was populated with brittle features typically observed in the fast fracture zone but with evidence of striations still traversing the surface. The transition from the crack propagation to fast fracture zone, traced in Figure 26, was indicated by the presence of tightly spaced striations. Specimen fractured with a 57% of UTS loading at 6.79×10^5 cycles.

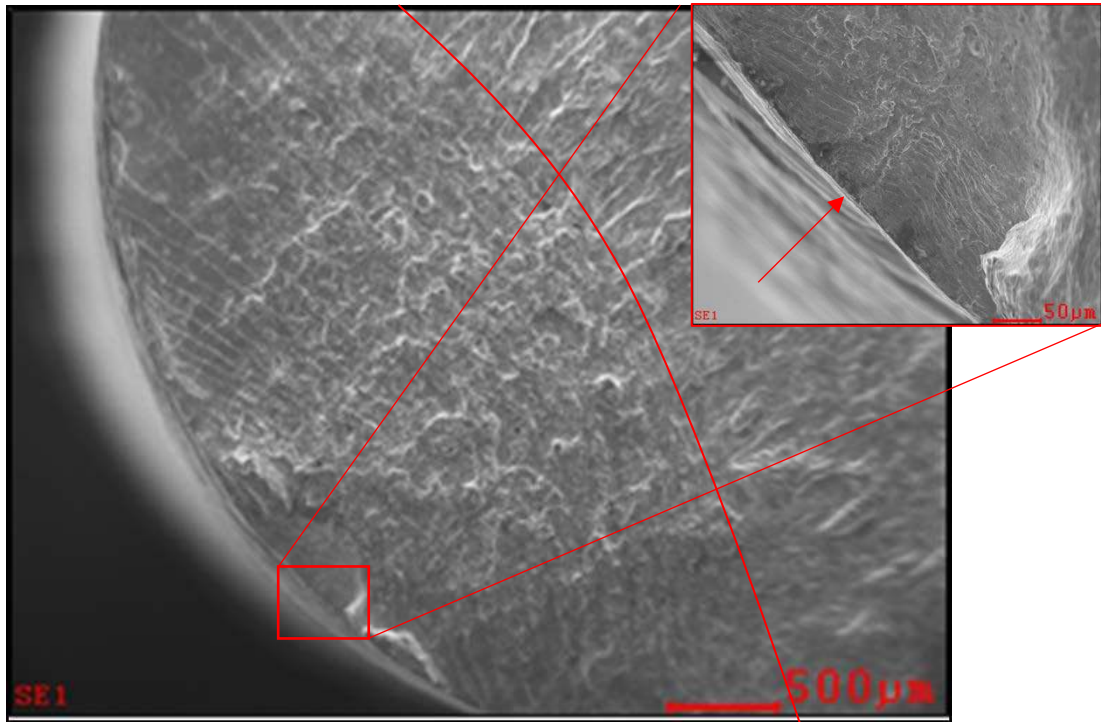


Figure 26: 100.0 J/mm³ energy density 0° orientation fatigue fracture. In magnified image red arrow points to crack initiation site, a small surface defect. Transition from crack propagation to fast fracture is outlined.

Crack initiation for the medium energy density 45° orientation came from a surface defect which fractured over to a large lack of fusion defect near the surface. The lack of fusion defect was the source of most of the crack propagation zone circled in Figure 27. Crack propagation was atypical by forming in a narrow oval running into the specimen rather than forming a classic half-moon radiating out from the crack initiation site. Specimen fractured with a 55% of UTS loading at $9.47 \cdot 10^5$ cycles.

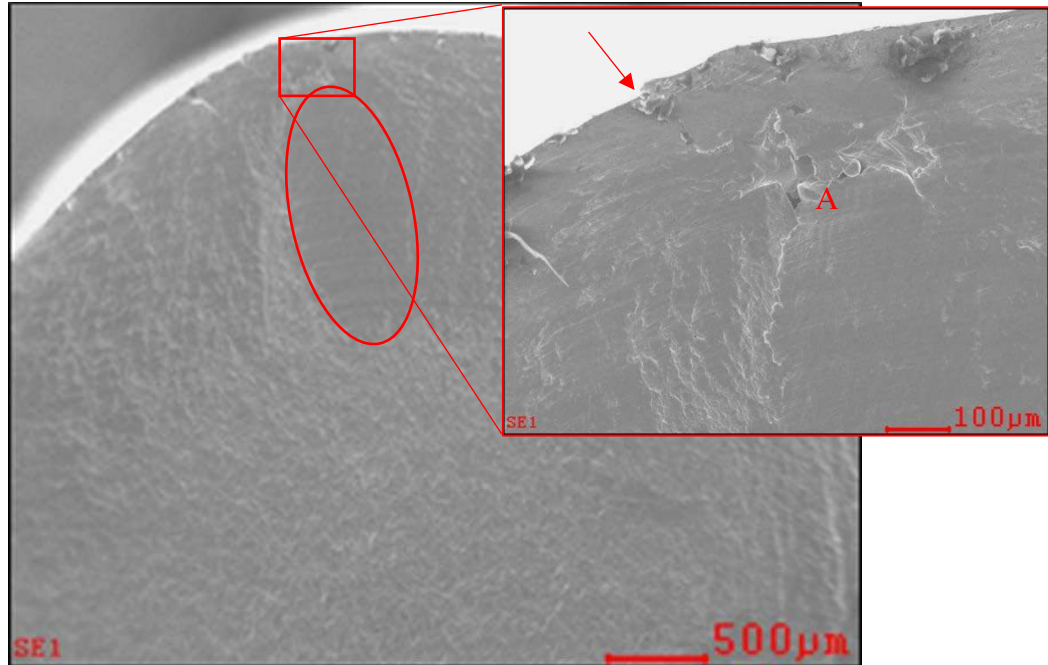


Figure 27: 100.0 J/mm³ energy density 45° orientation fatigue fracture. In magnified image red arrow points to crack initiation site, a small surface defect, which broke over to a large lack of fusion defect, A. Crack propagation zone is a non-typical shape, an approximate oval, enclosed in oval.

Crack initiation for the transverse medium energy density specimen came from a complex of surface defects at the edge of the specimen magnified in Figure 28. Due to the large number of crack initiation sites near each other, the initial crack propagation zone had striations that oriented in multiple directions amidst many, small, secondary cracks. The overall crack propagation zone was indistinct at low magnification. The transition to fast fracture could be identified at high magnification by a band of faint striations marking the end of the crack propagation zone as shown in Figure 29. Specimen fractured with a 54% of UTS loading at 1.66×10^6 cycles.

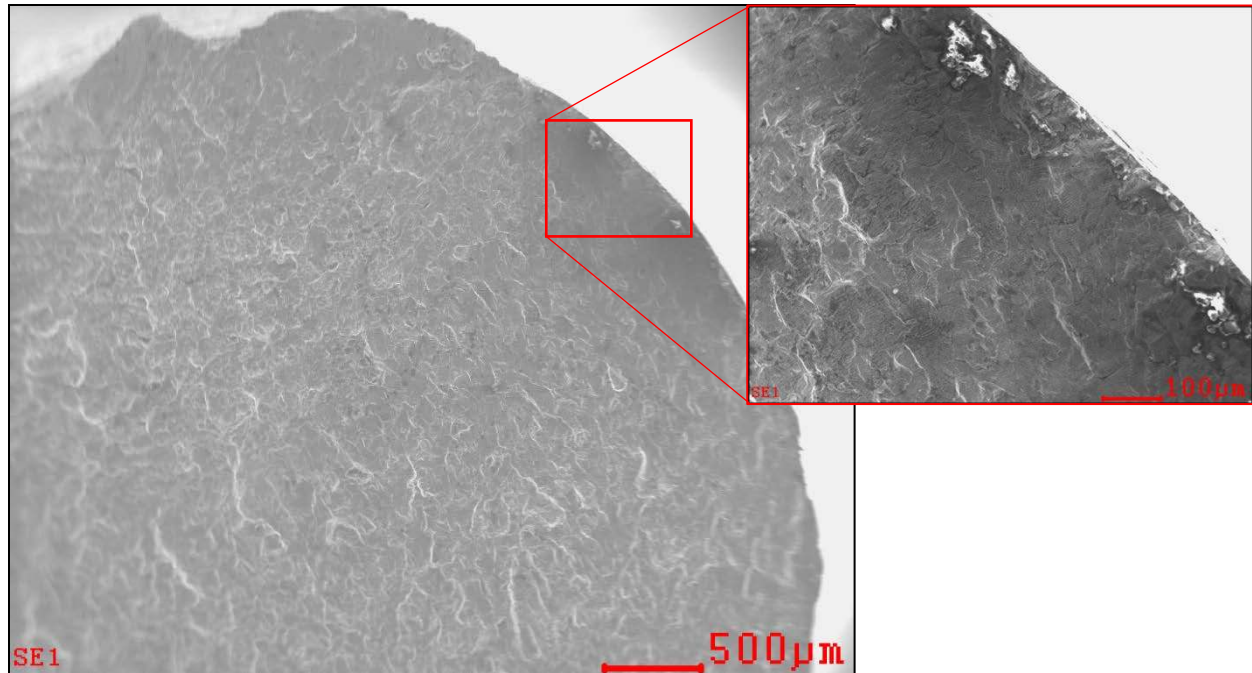


Figure 28: 100.0 J/mm³ energy density 90° orientation fatigue fracture. Magnified image highlights complex of crack initiation sites along specimen edge and first portion of crack propagation zone.

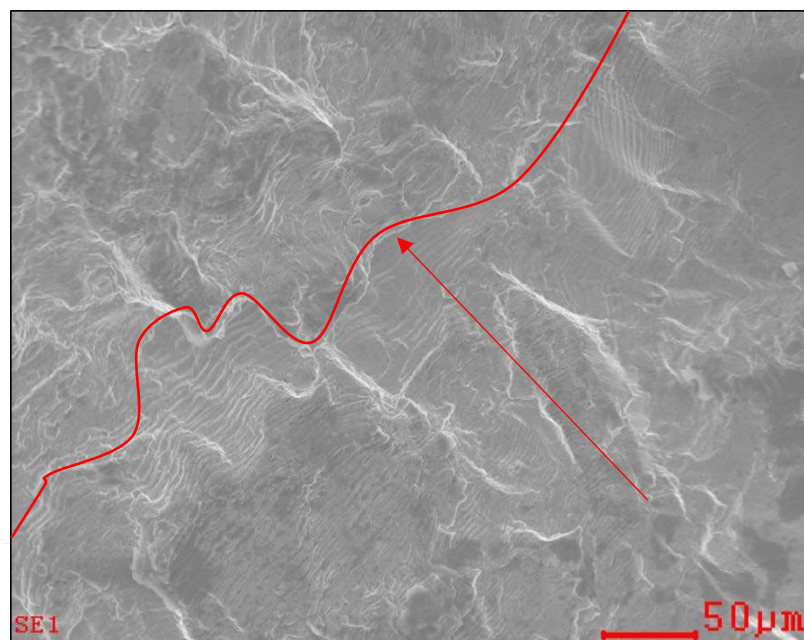


Figure 29: 100.0 J/mm³ energy density 90° orientation fatigue fracture. Transition zone between crack propagation zone and fast fracture zone approximately outlined. Arrow indicates direction of crack propagation.

4.3.6. High Energy Density Fatigue Fractography

The high energy density longitudinal specimen initiated cracking from a pair of defects at the specimen edge indicated by arrows A and B in Figure 30. The crack propagation zone is approximately 400 μm at its deepest section. Specimen fractured with a 60% of UTS loading at 3.90×10^5 cycles.

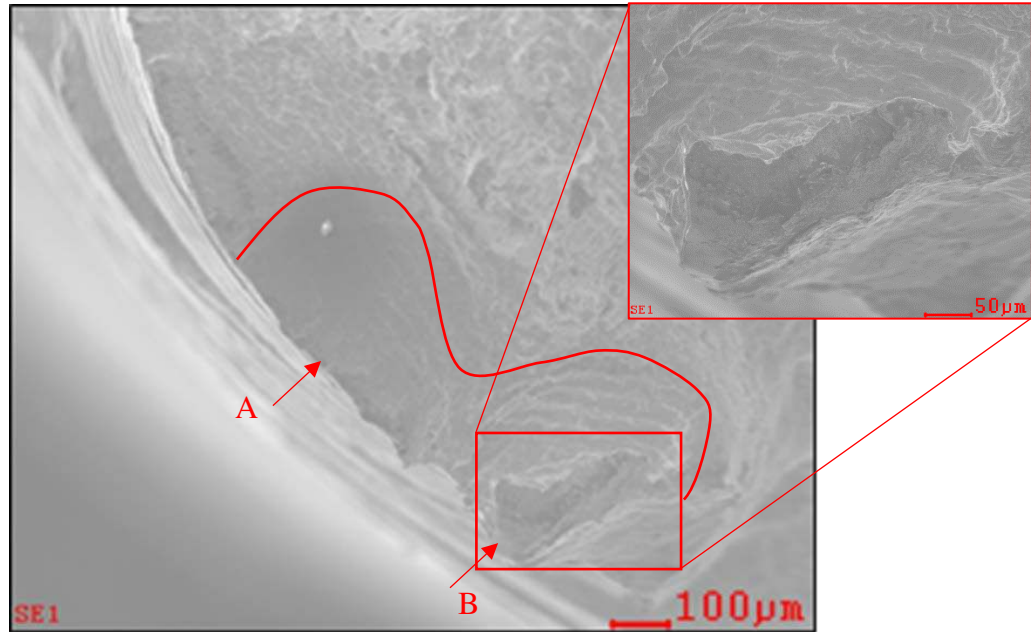


Figure 30: 187.6 J/mm³ energy density 0° orientation fatigue fracture. Red arrows point to a pair of adjacent crack initiation sites. Initiation site A is a small surface defect, site B a large surface defect, outer surface is magnified. Approximate end of crack propagation zone is outlined.

The final fracture zone, shown in Figure 31, abuts to a large uprising on the fracture surface. The zone differed somewhat from the typically observed by having a series of flat planar steps down to the specimen edge. A large angular void was observed on the final fracture zone also not typically observed in this study.

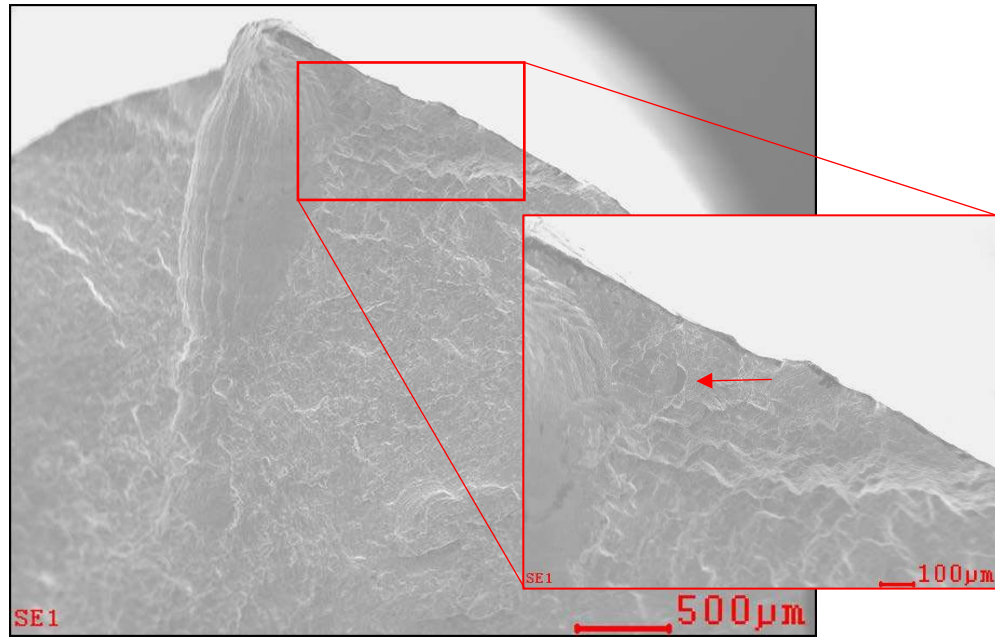


Figure 31: 187.6 J/mm³ energy density 0° orientation fatigue fracture. Final fracture zone with brittle features along cleavage planes. Arrow in magnified image is a large irregular shaped void.

The 45° orientation high energy density specimen did not have a distinct crack initiation site or propagation zone. Figure 32 highlights a surface feature that resembles striations but which run perpendicular to the direction of propagation that should occur based on the axis of loading. The most likely final fracture zone is shown in Figure 33 where the fast fracture zone transitions to a flat planar fracture surface lacking striations or other signs of crack propagation. Specimen fractured with a 60% of UTS loading at $1.37 \cdot 10^5$ cycles.

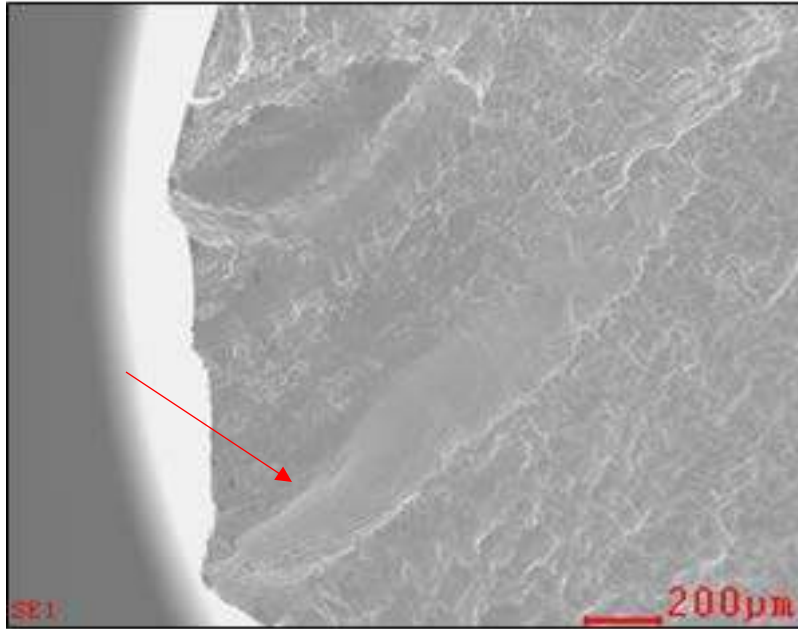


Figure 32: 187.6 J/mm³ energy density 45° orientation fatigue fracture. Red arrow points toward a surface feature reminiscent of striations but in a direction perpendicular to expected direction.

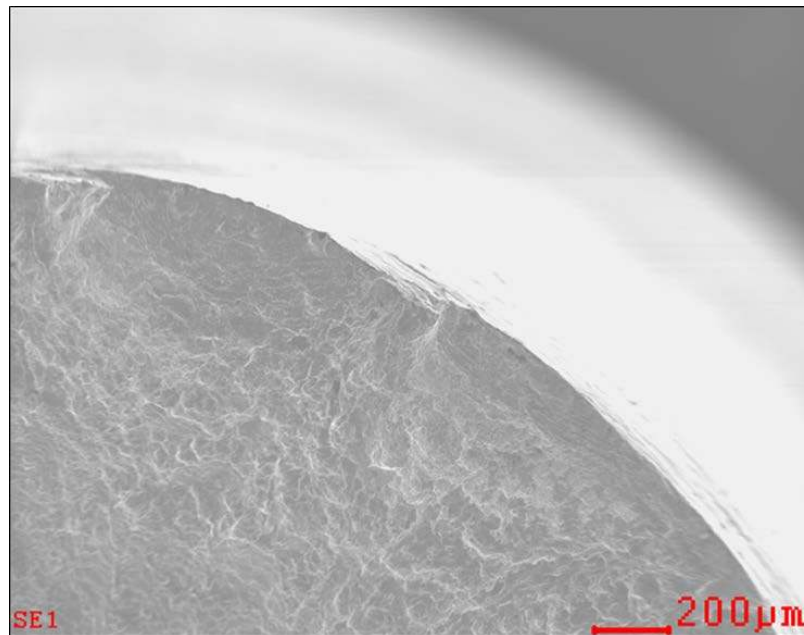


Figure 33: 187.6 J/mm³ energy density 45° orientation fatigue fracture. Proposed final fracture zone indicated by transition to flat planar fracture surface lacking striations.

The transverse high energy density specimen had crack initiation from a surface defect indicated to by arrow in Figure 34. Crack initiation occurred below the level of the primary

fracture surface. The crack propagation zone went approximately 700 μm into the specimen before transitioning to brittle fast fracture. Specimen fractured with a 65% of UTS loading at 2.23×10^4 cycles.

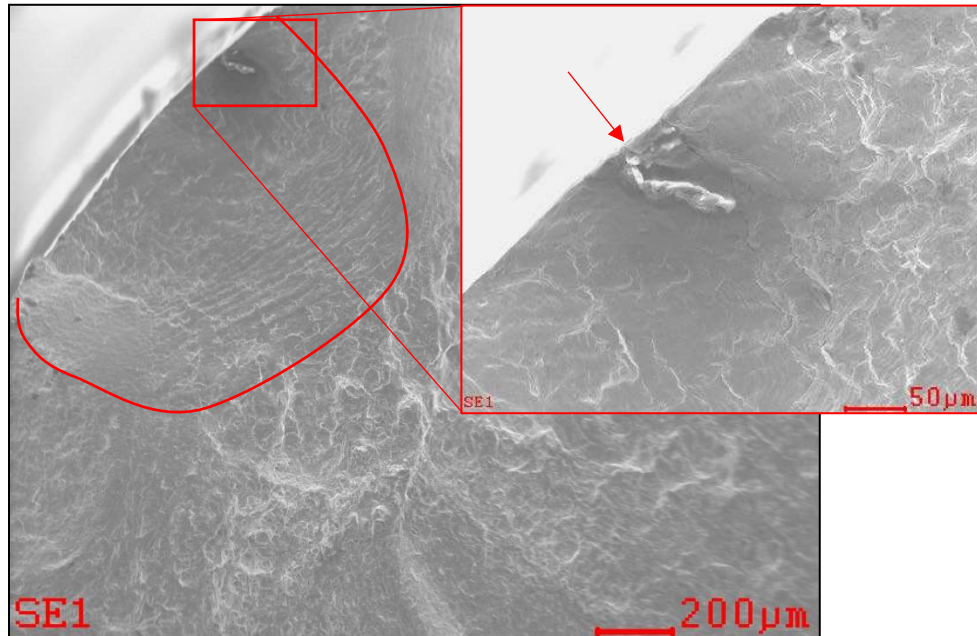


Figure 34: 187.6 J/mm³ energy density 90° orientation fatigue fracture. Red arrow in magnified image points to surface defect which initiated cracking. Line traces approximate end of crack propagation zone.

4.4. Microstructural Analysis

The apparent melt track area for the low energy density specimens was greatest at the longitudinal orientation and reduced as the build angle increased to the transverse orientation. The medium energy density specimens had an observed melt track area that was maximum for the transverse orientation followed by the longitudinal and lowest at the 45° orientation. The high energy density specimens had an apparent melt track area that became progressively larger as the orientation increased from longitudinal to transverse. The standard deviation exceeded the mean result for every specimen examined except for the medium energy density transverse orientation.

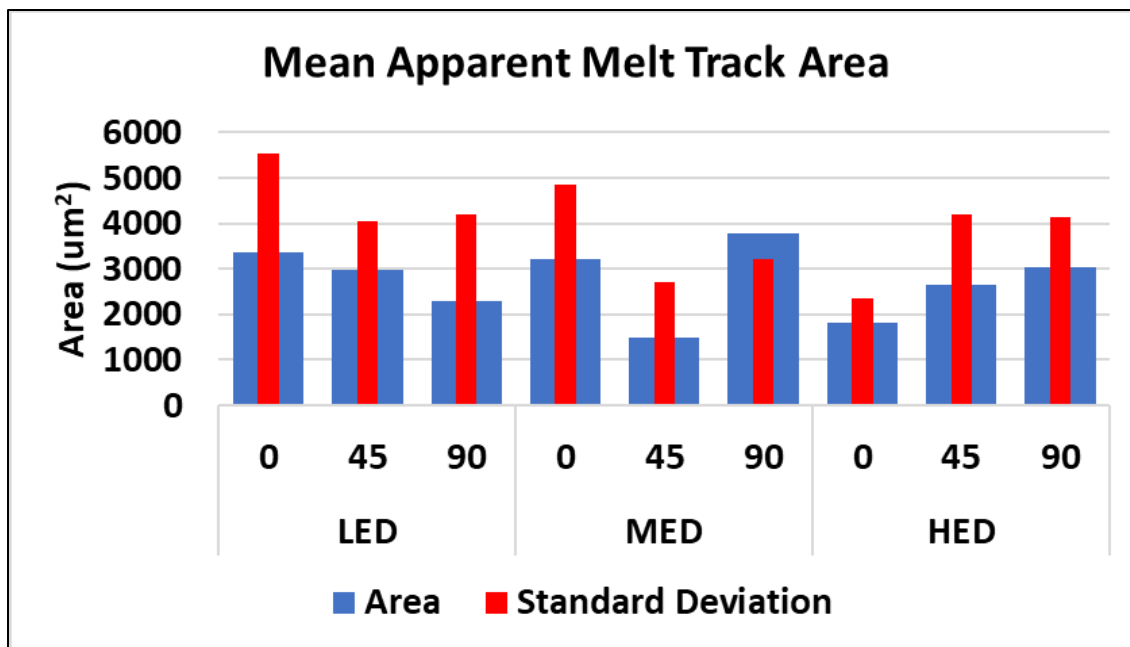


Figure 35: Mean apparent melt track area and standard deviation for the low, medium, and high energy densities.

The low energy density specimens possess a similar dendrite area with a maximum difference between longitudinal and 45° orientation specimens being 10%. The average of the low energy density dendrite area was $0.85 \mu\text{m}^2$. The mean dendrite area for the medium energy density had the smallest dendrites being for the transverse orientation followed by the longitudinal and the 45° orientation possessing the largest. High energy density specimens had a mean dendrite area that was smallest at the 45° orientation followed by the 90° orientation and the greatest being the longitudinal orientation. The standard deviation was greater than 50% of the mean dendrite area for all but the longitudinal medium energy density specimen. Standard deviation exceeded the mean dendrite area for the 45° and transverse orientation medium energy density specimens, and the longitudinal orientation high energy density specimen.

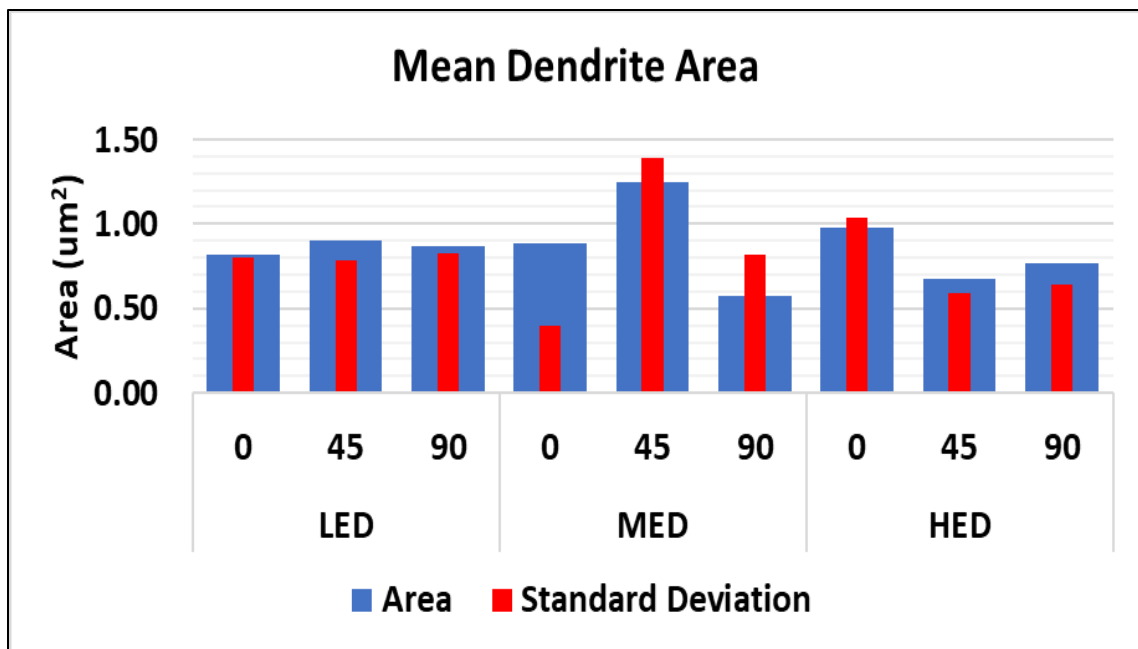


Figure 36: Mean dendrite area and standard deviation for the low, medium, and high energy densities

5. DISCUSSION

Use of limited specimens allowed for the development of trends between the UTS and high cycle fatigue limit with the energy density. Fractography revealed material properties that impacted the mechanical behavior of the test specimens.

5.1. Ultimate Tensile Strength

Previous work (9, 22) has indicated that if the axis of loading is perpendicular to the melt track layers, delamination occurs and leads to reduced strength. The degree to which this occurs is linked to the quality of fusion between melt track layers. Poor interlayer fusion arises from lack of penetration or residual defects from the previously deposited layer of melt tracks. Fractography revealed the low energy density specimens to have poor fusion which supports the low transverse UTS. The medium energy density having the optimum UTS in the study indicates that fusion between melt track layers was good, this only partially supported by the fractography. With the exception for the 45° orientation, the medium energy density fractured with a moderate ductility. The high energy density specimens were observed to have a moderate ductility and low volume of irregular voids, and yet had a lower UTS in the transverse orientation than the medium energy density specimens. This indicates that either there were defects that were not observed in fractography or that another mechanism was in play that reduced the UTS.

5.2. High Cycle Fatigue

The low and inconsistent fatigue limit of the low energy density specimens is attributed to a large volume of defects supported by the fractography results where lack of fusion defects contributed strongly to crack initiation and propagation. The medium energy specimens had the best fatigue limit in this study which indicates that 100.0 J/mm³ was sufficient to achieve a good fusion and not generate an excessive volume of defects. The relatively low defect volume

observed in fractography supports this though lack of fusion was observed. The high energy density specimen having a low but consistent fatigue limit indicates that there was an increase in defects compared to the medium energy density. The fractography did not reveal a higher interior defect volume for the high energy density specimens. The reduction in fatigue limit could potentially be attributed to a reduction in surface quality.

5.3. Fractography

It is theorized that the tensile specimens fractured with a flat fracture surface due to a large volume of defects. When the defect volume exceeded some critical amount the loss in ductility prevented the specimens from being able to shear. Related is that as the volume of defects decreased the features indicating a greater ductility increased. The volume of defects observed did not have a significant impact on the UTS except for the transverse orientation. The high volume of lack of fusion defects observed with the low energy density specimens contributed to a significant reduction in transverse UTS. The volume of defects observed with the medium energy density was not the primary contributing factor to UTS. This is based on the medium energy density having a greater observed volume of internal defects, but a greater UTS than the high energy density.

The low energy density specimens for both the tensile and fatigue fractography were observed to have evidence of lack of fusion between individual melt tracks and melt track layers; most readily observed in Figures 12 and 13. The high volume of lack of fusion defects proves 55.6 J/mm^3 is insufficient to achieve good fusion. The poor fusion did not impact the UTS except for under transverse loading.

5.4. Microstructural Analysis

The microstructural analysis results were aberrant and cannot be considered reliable. The apparent melt track areas were not consistent with results expected based on current understanding of melt track formation principles. Under current theory as the energy density increases the melt track area is expected to increase. Therefore, the low energy density would be expected to have the smallest average melt tracks and the high energy density the largest. Further the melt track size results form no clear correlation with the parameters used for construction, the UTS, or high cycle fatigue. Dendrite size similarly doesn't follow the expected trend based on established grain growth theory. It would be expected that as the heat input to the melt increases the solidification time and by extension dendrite size would increase. The high standard deviation for the microstructural analysis makes the mean results unreliable. With an increase in specimens examined the deviation from the mean should decrease.

6. CONCLUSIONS

The optimum energy density in this study was 100.0 J/mm^3 . This agrees with other research indicating 104 J/mm^3 as an optimum energy density for LPBF processed 316L stainless steel. The best transverse UTS in the study was with the medium energy density related to it approaching optimum fusion. Moderate ductility was generally observed for the medium energy density specimens. The medium energy density had the best fatigue limit in the study with a relatively good resistance to crack propagation. There was evidence that the optimum energy density was not achieved since some lack of fusion defects were observed.

There was insufficient energy to achieve good fusion at 55.6 J/mm^3 . Lack of fusion defects and poorly fused melt tracks were prevalent. The high defect volume contributed to the poor transverse UTS, low inconsistent fatigue limit, and low ductility.

An excessive energy density based on its reduction in transverse UTS and fatigue limit occurred with 187.6 J/mm^3 . Good fusion was achieved given the low volume of lack of fusion defects observed during fractography. Since a low volume of internal voids were observed the reduction in fatigue limit most likely resulted from a reduced surface quality.

The defect volume did not have an observed effect on the UTS except in the transverse orientation. The volume of defects did have an impact on the observed ductility of the specimens. This indicates that while defect volume is important to the tensile properties of LPBF components it may not be the principle factor in fracture under static loading. The quality of fusion is indicated as being the controlling factor for the UTS when loading perpendicular to the melt track layers.

The microstructural analysis results were too scattered for consideration in determining how they affect mechanical properties. More specimens would be required so that the coefficient

of variation could be reduced to allow for establishing the correlations that exist between the microstructure and mechanical properties.

7. RECOMENDATIONS

Future research should test specimens printed with energy densities ranging from 100 J/mm³ to 110 J/mm³ and incorporate the following studies.

1. A full fatigue study performed with enough specimens to allow for at least triplicate testing to form an average and generate a S-N curve. It would be better to test each unique combination of variables ten times to better account for scatter inherent to fatigue testing.
2. An in-depth study of the melt track size using more specimens should be performed to determine the correlation between the apparent melt track size and mechanical properties.
3. An EBSD study to determine the size and growth direction of grains.

8. REFERENCES

- [1] Wohlers, Terry, and Tim Gornet. "History of additive manufacturing." Wohlers report 24.2014 (2014): 118.
- [2] R. J. Herbert, "Viewpoint: Metallurgical aspects of powder bed metal additive manufacturing," *Journal of Material Science*, no. 51, pp. 1165-1175, 2016.
- [3] Sun, Zhongji, et al. "Selective laser melting of stainless steel 316L with low porosity and high build rates." *Materials & Design* 104 (2016): 197-204.
- [4] Marya, Manuel, et al. "Microstructural development and technical challenges in laser additive manufacturing: case study with a 316L industrial part." *Metallurgical and Materials Transactions B* 46.4 (2015): 1654-1665.
- [5] Gu, D. D., et al. "Laser additive manufacturing of metallic components: materials, processes and mechanisms." *International materials reviews* 57.3 (2012): 133-164.
- [6] Song, Bo, et al. "Differences in microstructure and properties between selective laser melting and traditional manufacturing for fabrication of metal parts: A review." *Frontiers of Mechanical Engineering* 10.2 (2015): 111-125.
- [7] Zhong, Yuan, et al. "Intragranular cellular segregation network structure strengthening 316L stainless steel prepared by selective laser melting." *Journal of Nuclear Materials* 470 (2016): 170-178.
- [8] Guo, Nannan, and Ming C. Leu. "Additive manufacturing: technology, applications and research needs." *Frontiers of Mechanical Engineering* 8.3 (2013): 215-243.
- [9] Wang, Di, et al. "Investigation of crystal growth mechanism during selective laser melting and mechanical property characterization of 316L stainless steel parts." *Materials & Design* 100 (2016): 291-299.

- [10] Cherry, J. A., et al. "Investigation into the effect of process parameters on microstructural and physical properties of 316L stainless steel parts by selective laser melting." *The International Journal of Advanced Manufacturing Technology* 76.5-8 (2015): 869-879.
- [11] Kamath, Chandrika, et al. "Density of additively-manufactured, 316L SS parts using laser powder-bed fusion at powers up to 400 W." *The International Journal of Advanced Manufacturing Technology* 74.1-4 (2014): 65-78.
- [12] Yasa, Evren, and Jean-Pierre Kruth. "Application of laser re-melting on selective laser melting parts." *Advances in Production engineering and Management* 6.4 (2011): 259-270.
- [13] Carlton, Holly D., et al. "Damage evolution and failure mechanisms in additively manufactured stainless steel." *Materials Science and Engineering: A* 651 (2016): 406-414.
- [14] Matthews, Manyalibo J., et al. "Denudation of metal powder layers in laser powder bed fusion processes." *Acta Materialia* 114 (2016): 33-42.
- [15] Schade, Christopher T., Thomas F. Murphy, and Chris Walton. "Development of atomized powders for additive manufacturing." *Powder Metallurgy Word Congress*, Accessed on 2nd July. 2014.
- [16] Yadroitsev, I., et al. "Energy input effect on morphology and microstructure of selective laser melting single track from metallic powder." *Journal of Materials Processing Technology* 213.4 (2013): 606-613.

- [17] Manvatkar, V., A. De, and T. DebRoy. "Heat transfer and material flow during laser assisted multi-layer additive manufacturing." *Journal of Applied Physics* 116.12 (2014): 124905.
- [18] Masmoudi, Amal, Rodolphe Bolot, and Christian Coddet. "Investigation of the laser– powder–atmosphere interaction zone during the selective laser melting process." *Journal of Materials Processing Technology* 225 (2015): 122-132.
- [19] Khairallah, Saad A., and Andy Anderson. "Mesoscopic simulation model of selective laser melting of stainless steel powder." *Journal of Materials Processing Technology* 214.11 (2014): 2627-2636.
- [20] Mower, Todd M., and Michael J. Long. "Mechanical behavior of additive manufactured, powder-bed laser-fused materials." *Materials Science and Engineering: A* 651 (2016): 198-213.
- [21] Khairallah, Saad A., et al. "Laser powder-bed fusion additive manufacturing: Physics of complex melt flow and formation mechanisms of pores, spatter, and denudation zones." *Acta Materialia* 108 (2016): 36-45.
- [22] Rawn, Penn. *3D Printing of 316L Stainless Steel and Its Effect on Microstructure and Mechanical Properties*. Diss. Montana Tech of The University of Montana, 2017.
- [23] Kou, Sindo. *Welding metallurgy*. John Wiley & Sons, 2003.
- [24] Sander, J., et al. "Microstructure and properties of FeCrMoVC tool steel produced by selective laser melting." *Materials & Design* 89 (2016): 335-341.
- [25] Cheng, Bo, Subin Shrestha, and Kevin Chou. "Stress and deformation evaluations of scanning strategy effect in selective laser melting." *Additive Manufacturing* 12 (2016): 240-251.

- [26] Kruth, Jean-Pierre, et al. "Selective laser melting of iron-based powder." *Journal of materials processing technology* 149.1-3 (2004): 616-622.
- [27] Krauss, H., and M. F. Zaeh. "Investigations on manufacturability and process reliability of selective laser melting." *Physics Procedia* 41 (2013): 815-822.
- [28] Kajima, Yuka, et al. "Fatigue strength of Co–Cr–Mo alloy clasps prepared by selective laser melting." *journal of the mechanical behavior of biomedical materials* 59 (2016): 446-458.
- [29] Brooks, Charlie R., and Ashok Choudhury. *Failure analysis of engineering materials*. New York: McGraw-Hill, 2002.
- [30] Akita, Masayuki, et al. "Defect-dominated fatigue behavior in type 630 stainless steel fabricated by selective laser melting." *Materials Science and Engineering: A* 666 (2016): 19-26.
- [31] Yadroitsev, Ihar. *Selective laser melting: Direct manufacturing of 3D-objects by selective laser melting of metal powders*. Lambert Academic Publishing, 2009.
- [32] Gu, Hengfeng, et al. "Effects of powder variation on the microstructure and tensile strength of Ti6Al4V parts fabricated by selective laser melting." *Proceedings of the 25th Annual International Solid Freeform Fabrication Symposium, Austin, TX, USA*. 2014.
- [33] Strondl, Annika, et al. "Characterization and control of powder properties for additive manufacturing." *Jom* 67.3 (2015): 549-554.
- [34] King, Wayne E., et al. "Observation of keyhole-mode laser melting in laser powder-bed fusion additive manufacturing." *Journal of Materials Processing Technology* 214.12 (2014): 2915-2925.

- [35] Parry, L., I. A. Ashcroft, and Ricky D. Wildman. "Understanding the effect of laser scan strategy on residual stress in selective laser melting through thermo-mechanical simulation." *Additive Manufacturing* 12 (2016): 1-15.
- [36] Dowling, Norman E. *Mechanical behavior of materials: engineering methods for deformation, fracture, and fatigue*. Pearson, 2012.
- [37] Benyounis, K. Y., A. G. Olabi, and M. S. J. Hashmi. "Effect of laser welding parameters on the heat input and weld-bead profile." *Journal of materials processing technology* 164 (2005): 978-985.
- [38] Stugelmayer, Edward. "Characterization of Process Induced Defects in Laser Powder Bed Fusion Processed AlSi10Mg Alloy." (2018).
- [39] Strano, Giovanni, et al. "Surface roughness analysis, modelling and prediction in selective laser melting." *Journal of Materials Processing Technology* 213.4 (2013): 589-597.
- [40] ASTM International, "ASTM E8/E8M-16a," in *Standard Test Methods for Tension Testing of Metallic Materials*, West Conshohocken, Pa, ASTM International, (2016).
- [41] "EOS M 290." *EOS Industrial 3D Printing - Process, Method and Benefits*, www.eos.info/eos-m290.
- [42] Fatigue dynamics Inc., Model RBF-200 Instruction Manual, Pg. 5. 1995.

9. Appendix A: Tabulated Mechanical Test Results

Table IV: Tabulated Average UTS Results

Energy Density	Orientation	Average UTS (psi)	Average UTS (MPa)	Standard Deviation	Coefficient of Variation (%)
55.6 J/mm ³	0 Deg.	88517	610	5.00	1
	45 Deg.	88457	610	3.28	1
	90 Deg.	71485	493	12.56	3
100.0 J/mm ³	0 Deg.	91229	629	0.18	< 1
	45 Deg.	87454	603	2.66	< 1
	90 Deg.	93695	646	0.10	< 1
187.6 J/mm ³	0 Deg.	90041	621	1.25	< 1
	45 Deg.	88068	607	0.89	< 1
	90 Deg.	81941	565	3.20	1

Table V: Tabulated Fatigue Test Results

Orientation	Build Set					
	Low Energy Density (55.6J/mm ³)		Medium Energy Density (100.0 J/mm ³)		High Energy Density (187.6 J/mm ³)	
	% UTS	Cycles Achieved	% UTS	Cycles Achieved	% UTS	Cycles Achieved
0	55	1.62E+06	55	1.35E+07	55	1.29E+07
	60	1.53E+05	60	7.50E+06	60	3.90E+05
	65	1.95E+04	65	1.33E+05	65	2.38E+04
45	55	1.66E+05	56	1.11E+07	55	1.05E+07
	60	2.41E+05	60	1.03E+07	60	1.37E+05
	65	2.00E+04	65	1.01E+07	65	1.69E+04
90	55	1.03E+07	55	1.09E+07	55	1.01E+07
	60	4.65E+06	58	1.14E+07	60	1.50E+05
	65	1.00E+05	65	1.77E+04	65	2.23E+04

10. Appendix B: Example Drawing of Moderate Ductility Tensile Fracture

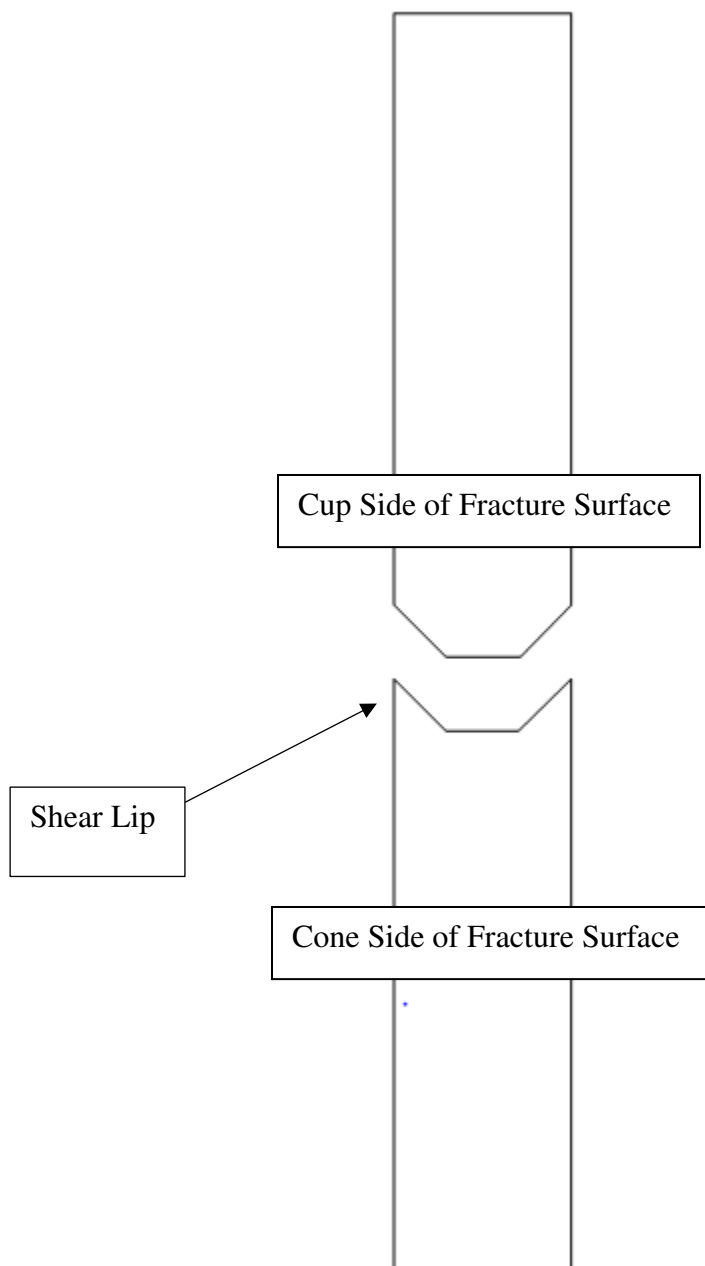


Figure 37: Example cross section diagram of a moderate ductility tensile fracture.

11. Appendix C: Tabulated Statistics for Apparent Melt Track Size

Table VI: Low energy density 0° orientation apparent melt track area, length, and breadth statistics for the 'XY' sample.

55.6 J/mm ³ 0° Apparent Melt Track Size 'XY'			
Statistic	Area(μm ²)	Length(μm)	Breadth(μm)
Counts (No Units)	1658	1658	1658
Mean	3161.2	87.9	42.6
Standard Deviation	4944.8	82.5	35.4
Coefficient of Variation	0.6	1.1	1.2
Minimum	4.7	2.9	1.2
Q1	278.6	29.1	16.3
Median	1359.5	67.5	34.3
Q3	3934.2	113.5	58.2
Maximum	34106.4	571.9	230.4

Table VII: Low energy density 0° orientation apparent melt track area, length, and breadth statistics for the 'Z' sample.

55.6 J/mm ³ 0° Apparent Melt Track Size 'Z'			
Statistic	Area(μm ²)	Length(μm)	Breadth(μm)
Counts (No Units)	1880	1880	1880
Mean	3551.5	87.0	46.7
Standard Deviation	6110.2	76.5	41.5
Coefficient of Variation	1.7	0.9	0.9
Minimum	3.4	2.3	0.6
Q1	362.5	34.9	18.0
Median	1241.2	65.2	34.3
Q3	3994.4	115.3	65.2
Maximum	66014.5	677.8	405.5

Table VIII: Low energy density 45° orientation apparent melt track area, length, and breadth statistics for the 'XY' sample.

55.6 J/mm ³ 45° Apparent Melt Track Size 'XY'			
Statistic	Area(μm ²)	Length(μm)	Breadth(μm)
Counts (No Units)	7430	7430	7430
Mean	3484.3	65.5	39.4
Standard Deviation	4940.6	45.6	28.3
Coefficient of Variation	1.4	0.7	0.7
Minimum	6.4	3.5	0.6
Q1	588.7	33.1	18.6
Median	1603.1	54.5	31.3
Q3	4385.4	86.4	54.5
Maximum	36259.9	335.2	152.0

Table IX: Low energy density 45° orientation apparent melt track area, length, and breadth statistics for the 'Z' sample.

55.6 J/mm ³ 45° Apparent Melt Track Size 'Z'			
Statistic	Area(μm ²)	Length(μm)	Breadth(μm)
Counts (No Units)	3517	3517	3517
Mean	2176.7	71.2	36.9
Standard Deviation	3180.3	56.4	30.5
Coefficient of Variation	1.5	0.8	0.8
Minimum	3.4	2.3	0.6
Q1	205.5	27.3	12.8
Median	829.0	57.0	27.9
Q3	2859.1	102.4	53.5
Maximum	30797.8	382.3	220.5

Table X: Low energy density 90° orientation apparent melt track area, length, and breadth statistics for the 'XY' sample.

55.6 J/mm ³ 90° Apparent Melt Track Size 'XY'			
Statistic	Area(μm ²)	Length(μm)	Breadth(μm)
Counts (No Units)	2097	2097	2097
Mean	3004.7	80.3	43.5
Standard Deviation	5214.0	69.4	37.1
Coefficient of Variation	1.7	0.9	0.9
Minimum	3.4	2.3	0.6
Q1	260.3	30.3	15.7
Median	1066.7	62.3	32.6
Q3	3621.7	109.7	62.3
Maximum	64873.4	609.7	296.7

Table XI: Low energy density 90° orientation apparent melt track area, length, and breadth statistics for the 'Z' sample.

55.6 J/mm ³ 90° Apparent Melt Track Size 'Z'			
Statistic	Area(μm ²)	Length(μm)	Breadth(μm)
Counts (No Units)	1908	1908	1908
Mean	1585.9	59.9	33.1
Standard Deviation	3177.5	49.2	27.4
Coefficient of Variation	2.0	0.8	0.8
Minimum	3.4	2.3	1.2
Q1	211.8	26.8	14.0
Median	596.5	46.5	25.6
Q3	1543.4	76.9	43.6
Maximum	55851.7	418.9	254.3

Table XII: Medium energy density 0° orientation apparent melt track area, length, and breadth statistics for the 'XY' sample.

100.0 J/mm ³ 0° Apparent Melt Track Size 'XY'			
Statistic	Area(μm ²)	Length(μm)	Breadth(μm)
Counts (No Units)	1529	1529	1529
Mean	4435.4	104.5	59.2
Standard Deviation	5067.7	64.8	35.4
Coefficient of Variation	0.9	1.6	1.7
Minimum	4.1	2.3	1.2
Q1	1073.4	59.3	32.6
Median	2539.9	90.2	51.8
Q3	6043.1	135.0	80.3
Maximum	37195.3	447.4	225.7

Table XIII: Medium energy density 0° orientation apparent melt track area, length, and breadth statistics for the 'Z' sample.

100.0 J/mm ³ 0° Apparent Melt Track Size 'Z'			
Statistic	Area(μm ²)	Length(μm)	Breadth(μm)
Counts (No Units)	2666.0	2666.0	2666.0
Mean	3136.5	90.1	43.7
Standard Deviation	4606.2	71.2	33.9
Coefficient of Variation	1.7	0.8	0.8
Minimum	3.4	2.3	0.6
Q1	354.7	36.7	17.5
Median	1420.1	73.9	36.0
Q3	4019.7	123.9	61.7
Maximum	44515.0	478.3	233.0

Table XIV: Medium energy density 45° orientation apparent melt track area, length, and breadth statistics for the 'XY' sample.

100.0 J/mm ³ 45° Apparent Melt Track Size 'XY'			
Statistic	Area(μm ²)	Length(μm)	Breadth(μm)
Counts (No Units)	3989	3989	3989
Mean	1203.0	50.9	29.8
Standard Deviation	2132.3	37.3	20.6
Coefficient of Variation	1.8	0.7	0.7
Minimum	2.2	1.9	0.5
Q1	249.8	26.8	16.0
Median	561.1	41.4	24.0
Q3	1327.8	63.4	38.1
Maximum	56105.3	564.9	215.3

Table XV: Medium energy density 45° orientation apparent melt track area, length, and breadth statistics for the 'Z' sample.

100.0 J/mm ³ 45° Apparent Melt Track Size 'Z'			
Statistic	Area(μm ²)	Length(μm)	Breadth(μm)
Counts (No Units)	4573	4573	4573
Mean	1765.5	68.9	29.2
Standard Deviation	3277.8	62.4	26.2
Coefficient of Variation	1.9	0.9	0.9
Minimum	3.4	2.3	0.6
Q1	191.3	27.9	11.6
Median	525.4	48.9	19.8
Q3	1610.3	89.0	37.2
Maximum	30227.1	639.4	220.5

Table XVI: Medium energy density 90° orientation apparent melt track area, length, and breadth statistics for the 'XY' sample.

100.0 J/mm ³ 90° Apparent Melt Track Size 'XY'			
Statistic	Area(μm ²)	Length(μm)	Breadth(μm)
Counts (No Units)	2871	2871	2871
Mean	2529.3	81.8	46.9
Standard Deviation	2322.2	41.5	23.0
Coefficient of Variation	0.9	0.5	0.5
Minimum	46.7	12.2	7.0
Q1	884.6	51.2	30.3
Median	1890.9	78.3	44.8
Q3	3267.7	104.1	60.4
Maximum	14093.9	254.8	147.2

Table XVII: Medium energy density 90° orientation apparent melt track area, length, and breadth statistics for the 'Z' sample.

100.0 J/mm ³ 90° Apparent Melt Track Size 'Z'			
Statistic	Area(μm ²)	Length(μm)	Breadth(μm)
Counts (No Units)	1808	1808	1808
Mean	3884.7	104.7	55.2
Standard Deviation	4096.2	56.2	28.7
Coefficient of Variation	0.9	1.9	1.9
Minimum	4.1	2.9	1.2
Q1	1116.7	63.4	32.0
Median	2472.8	94.5	50.6
Q3	5215.5	130.3	73.9
Maximum	30726.7	421.8	217.0

Table XVIII: High energy density 0° orientation apparent melt track area, length, and breadth statistics for the 'XY' sample.

187.6 J/mm ³ 0° Apparent Melt Track Size 'XY'			
Statistic	Area(μm ²)	Length(μm)	Breadth(μm)
Counts (No Units)	5808	5808	5808
Mean	1448.0	62.2	32.3
Standard Deviation	1956.0	42.2	19.0
Coefficient of Variation	1.4	0.7	0.6
Minimum	4.7	2.3	1.7
Q1	358.4	33.2	18.0
Median	782.6	51.8	27.3
Q3	1801.6	79.1	41.9
Maximum	40892.2	841.3	197.8

Table XIX: High energy density 0° orientation apparent melt track area, length, and breadth statistics for the 'Z' sample.

187.6 J/mm ³ 0° Apparent Melt Track Size 'Z'			
Statistic	Area(μm ²)	Length(μm)	Breadth(μm)
Counts (No Units)	3640	3640	3640
Mean	2188.3	78.7	37.4
Standard Deviation	2725.8	53.6	23.2
Coefficient of Variation	1.2	0.7	0.6
Minimum	3.4	2.3	0.6
Q1	453.5	40.1	19.8
Median	1200.0	66.9	32.0
Q3	2880.3	103.6	50.0
Maximum	37015.9	694.1	139.1

Table XX: High energy density 45° orientation apparent melt track area, length, and breadth statistics for the 'XY' sample.

187.6 J/mm ³ 45° Apparent Melt Track Size 'XY'			
Statistic	Area(μm ²)	Length(μm)	Breadth(μm)
Counts (No Units)	3058	3058	3058
Mean	9341.5	143.6	79.6
Standard Deviation	14621.0	123.2	53.8
Coefficient of Variation	1.6	0.9	0.7
Minimum	10.0	4.0	1.0
Q1	1453.3	64.0	40.0
Median	3999.5	109.0	65.0
Q3	11075.3	185.0	108.0
Maximum	225471.0	1142.0	427.0

Table XXI: High energy density 45° orientation apparent melt track area, length, and breadth statistics for the 'Z' sample.

187.6 J/mm ³ 45° Apparent Melt Track Size 'Z'			
Statistic	Area(μm ²)	Length(μm)	Breadth(μm)
Counts (No Units)	3916	3916	3916
Mean	2056.3	70.5	37.0
Standard Deviation	3326.0	56.9	25.8
Coefficient of Variation	1.6	0.8	0.7
Minimum	3.4	2.3	0.6
Q1	334.9	32.6	18.0
Median	946.8	55.9	30.8
Q3	2522.4	91.9	49.5
Maximum	67669.9	734.3	263.0

Table XXII: High energy density 90° orientation apparent melt track area, length, and breadth statistics for the 'XY' sample.

187.6 J/mm ³ 90° Apparent Melt Track Size 'XY'			
Statistic	Area(μm ²)	Length(μm)	Breadth(μm)
Counts (No Units)	3263	3263	3263
Mean	2383.2	84.3	34.7
Standard Deviation	3295.0	69.7	24.9
Coefficient of Variation	1.4	0.8	0.7
Minimum	3.4	2.3	0.6
Q1	276.2	32.0	14.5
Median	1043.6	64.6	28.5
Q3	3289.3	119.9	48.9
Maximum	38624.2	691.8	178.0

Table XXIII: High energy density 90° orientation apparent melt track area, length, and breadth statistics for the 'Z' sample.

187.6 J/mm ³ 90° Apparent Melt Track Size 'Z'			
Statistic	Area(μm ²)	Length(μm)	Breadth(μm)
Counts (No Units)	2578	2578	2578
Mean	3686.5	94.8	50.8
Standard Deviation	4983.7	64.9	33.8
Coefficient of Variation	0.7	1.5	1.5
Minimum	3.7	2.9	1.7
Q1	816.5	47.6	27.3
Median	2053.2	79.4	43.3
Q3	4903.3	123.1	68.1
Maximum	37381.5	390.4	233.3

12. Appendix D: Tabulated Statistics for Dendrite Size

Table XXIV: Low energy density 0° orientation dendrite area, length, and breadth statistics for the 'XY' sample.

55.6 J/mm ³ 0° Dendrite Size 'XY'			
Statistic	Area(μm ²)	Length(μm)	Breadth(μm)
Counts (No Units)	6867	6867	6867
Mean	1.03	1.63	0.91
Standard Deviation	1.08	0.84	0.46
Coefficient of Variation	0.96	1.93	1.98
Minimum	0.03	0.23	0.12
Q1	0.43	1.05	0.58
Median	0.73	1.45	0.81
Q3	1.25	1.98	1.11
Maximum	22.35	11.64	4.60

Table XXV: Low energy density 0° orientation dendrite area, length, and breadth statistics for the 'Z' sample.

55.6 J/mm ³ 0° Dendrite Size 'Z'			
Statistic	Area(μm ²)	Length(μm)	Breadth(μm)
Counts (No Units)	95960	95960	95960
Mean	0.61	1.23	0.73
Standard Deviation	0.52	0.54	0.31
Coefficient of Variation	0.85	0.44	0.43
Minimum	0.03	0.23	0.06
Q1	0.28	0.81	0.52
Median	0.47	1.11	0.70
Q3	0.78	1.51	0.87
Maximum	42.75	27.00	5.76

Table XXVI: Low energy density 45° orientation dendrite area, length, and breadth statistics for the 'XY' sample.

55.6 J/mm ³ 45° Dendrite Size 'XY'			
Statistic	Area(μm ²)	Length(μm)	Breadth(μm)
Counts (No Units)	89962	89962	89962
Mean	0.87	1.48	0.87
Standard Deviation	0.71	0.64	0.37
Coefficient of Variation	0.82	0.43	0.43
Minimum	0.03	0.23	0.06
Q1	0.41	0.99	0.58
Median	0.67	1.34	0.81
Q3	1.10	1.80	1.05
Maximum	9.61	11.58	4.01

Table XXVII: Low energy density 45° orientation dendrite area, length, and breadth statistics for the 'Z' sample.

55.6 J/mm ³ 45° Dendrite Size 'Z'			
Statistic	Area(μm ²)	Length(μm)	Breadth(μm)
Counts (No Units)	87014	87014	87014
Mean	0.94	1.52	0.89
Standard Deviation	0.85	0.69	0.41
Coefficient of Variation	0.90	0.45	0.46
Minimum	0.03	0.23	0.06
Q1	0.41	1.05	0.58
Median	0.70	1.40	0.81
Q3	1.16	1.86	1.11
Maximum	13.07	8.26	4.13

Table XXVIII: Low energy density 90° orientation dendrite area, length, and breadth statistics for the 'XY' sample.

55.6 J/mm ³ 90° Dendrite Size 'XY'			
Statistic	Area(μm ²)	Length(μm)	Breadth(μm)
Counts (No Units)	82563	82563	82563
Mean	1.05	1.62	0.95
Standard Deviation	1.12	0.88	0.53
Coefficient of Variation	1.06	0.54	0.55
Minimum	0.03	0.23	0.06
Q1	0.35	0.99	0.58
Median	0.70	1.45	0.87
Q3	1.34	2.04	1.22
Maximum	17.47	8.90	5.82

Table XXIX: Low energy density 90° orientation dendrite area, length, and breadth statistics for the 'Z' sample.

55.6 J/mm ³ 90° Dendrite Size 'Z'			
Statistic	Area(μm ²)	Length(μm)	Breadth(μm)
Counts (No Units)	95141	95141	95141
Mean	0.68	1.42	0.71
Standard Deviation	0.53	0.66	0.28
Coefficient of Variation	0.78	0.46	0.40
Minimum	0.03	0.23	0.06
Q1	0.35	0.99	0.52
Median	0.54	1.28	0.64
Q3	0.85	1.75	0.81
Maximum	14.8674	15.8836	4.0145

Table XXX: Medium energy density 0° orientation dendrite area, length, and breadth statistics for the 'XY' sample.

100.0 J/mm ³ 0° Dendrite Size 'XY'			
Statistic	Area(μm ²)	Length(μm)	Breadth(μm)
Counts (No Units)	127797	127797	127797
mean	0.51	1.12	0.67
Standard Deviation	0.34	0.42	0.24
Coefficient of Variation	1.51	2.70	2.76
Minimum	0.03	0.23	0.06
Q1	0.27	0.81	0.47
median	0.43	1.05	0.64
Q3	0.64	1.34	0.81
Maximum	23.33	8.32	6.11

Table XXXI: Medium energy density 0° orientation dendrite area, length, and breadth statistics for the 'Z' sample.

100.0 J/mm ³ 0° Dendrite Size 'Z'			
Statistic	Area(μm ²)	Length(μm)	Breadth(μm)
Counts (No Units)	109616	109616	109616
mean	0.64	1.25	0.75
Standard Deviation	0.45	0.49	0.29
Coefficient of Variation	1.43	2.57	2.60
Minimum	0.03	0.23	0.06
Q1	0.32	0.87	0.52
median	0.52	1.16	0.70
Q3	0.83	1.51	0.93
Maximum	6.08	4.89	3.08

Table XXXII: Medium energy density 45° orientation dendrite area, length, and breadth statistics for the 'XY' sample.

100.0 J/mm ³ 45° Dendrite Size 'XY'			
Statistic	Area(μm ²)	Length(μm)	Breadth(μm)
Counts (No Units)	47647	47647	47647
Mean	1.84	2.15	1.25
Standard Deviation	2.01	1.20	0.71
Coefficient of Variation	1.09	0.56	0.57
Minimum	0.03	0.23	0.06
Q1	0.59	1.28	0.76
Median	1.21	1.92	1.11
Q3	2.36	2.79	1.57
Maximum	41.19	13.27	6.63

Table XXXIII: Medium energy density 45° orientation dendrite area, length, and breadth statistics for the 'Z' sample.

100.0 J/mm ³ 45° Dendrite Size 'Z'			
Statistic	Area(μm ²)	Length(μm)	Breadth(μm)
Counts (No Units)	128142	128142	128142
Mean	0.65	1.29	0.74
Standard Deviation	0.76	0.71	0.39
Coefficient of Variation	1.17	0.55	0.53
Minimum	0.02	0.19	0.05
Q1	0.24	0.80	0.47
Median	0.43	1.13	0.66
Q3	0.78	1.60	0.89
Maximum	22.83	10.01	5.64

Table XXXIV: Medium energy density 90° orientation dendrite area, length, and breadth statistics for the 'XY' sample.

100.0 J/mm ³ 90° Dendrite Size 'XY'			
Statistic	Area(μm ²)	Length(μm)	Breadth(μm)
Counts (No Units)	91391	91391	91391
Mean	0.83	1.48	0.86
Standard Deviation	0.61	0.60	0.35
Coefficient of Variation	0.74	0.41	0.41
Minimum	0.03	0.23	0.12
Q1	0.41	1.05	0.64
Median	0.66	1.40	0.81
Q3	1.08	1.80	1.05
Maximum	6.40	5.06	3.03

Table XXXV: Medium energy density 90° orientation dendrite area, length, and breadth statistics for the 'Z' sample.

100.0 J/mm ³ 90° Dendrite Size 'Z'			
Statistic	Area(μm ²)	Length(μm)	Breadth(μm)
Counts (No Units)	82589	82589	82589
mean	0.95	1.54	0.92
Standard Deviation	0.87	0.73	0.43
Coefficient of Variation	0.99	0.49	0.48
Minimum	0.03	0.23	0.06
Q1	0.39	0.99	0.58
median	0.69	1.40	0.81
Q3	1.22	1.92	1.16
Maximum	13.42	7.62	4.71

Table XXXVI: High energy density 0° orientation dendrite area, length, and breadth statistics for the 'XY' sample.

187.6 J/mm ³ 0° Dendrite Size 'XY'			
Statistic	Area(μm ²)	Length(μm)	Breadth(μm)
Counts (No Units)	74201	74201	74201
Mean	1.19	1.69	0.98
Standard Deviation	1.45	0.97	0.58
Coefficient of Variation	1.22	0.57	0.59
Minimum	0.03	0.23	0.06
Q1	0.39	0.99	0.58
median	0.74	1.14	0.99
Q3	1.40	1.86	1.63
Maximum	26.02	26.02	26.02

Table XXXVII: High energy density 0° orientation dendrite area, length, and breadth statistics for the 'Z' sample.

187.6 J/mm ³ 0° Dendrite Size 'Z'			
Statistic	Area(μm ²)	Length(μm)	Breadth(μm)
Counts (No Units)	112975	112975	112975
Mean	0.76	1.40	0.80
Standard Deviation	0.63	0.61	0.34
Coefficient of Variation	0.82	0.43	0.43
Minimum	0.03	0.23	0.06
Q1	0.38	0.99	0.58
Median	0.60	1.28	0.76
Q3	0.95	1.69	0.99
Maximum	15.74	12.10	5.24

Table XXXVIII: High energy density 45° orientation dendrite area, length, and breadth statistics for the 'XY' sample.

187.6 J/mm ³ 45° Dendrite Size 'XY'			
Statistic	Area(μm ²)	Length(μm)	Breadth(μm)
Counts (No Units)	123216	123216	123216
Mean	0.66	1.29	0.74
Standard Deviation	0.63	1.27	0.73
Coefficient of Variation	0.47	0.52	0.28
Minimum	0.72	0.40	0.37
Q1	0.03	0.23	0.06
median	0.35	0.93	0.52
Q3	0.53	1.22	0.70
Maximum	0.83	1.57	0.87

Table XXXIX: High energy density 45° orientation dendrite area, length, and breadth statistics for the ‘Z’ sample.

187.6 J/mm ³ 45° Dendrite Size 'Z'			
Statistic	Area(μm ²)	Length(μm)	Breadth(μm)
Counts (No Units)	107254	107254	107254
Mean	0.68	1.29	0.78
Standard Deviation	0.56	0.56	0.34
Coefficient of Variation	0.81	0.44	0.44
Minimum	0.03	0.23	0.06
Q1	0.31	0.87	0.52
median	0.53	1.16	0.70
Q3	0.88	1.57	0.99
Maximum	8.70	6.57	3.61

Table XL: High energy density 90° orientation dendrite area, length, and breadth statistics for the ‘XY’ sample.


187.6 J/mm ³ 90° Dendrite Size 'XY'			
Statistic	Area(μm ²)	Length(μm)	Breadth(μm)
Counts (No Units)	85982	85982	85982
Mean	0.99	1.55	0.92
Standard Deviation	0.99	0.81	0.48
Coefficient of Variation	1.00	0.53	0.53
Minimum	0.03	0.23	0.06
Q1	0.35	0.93	0.58
Median	0.67	1.40	0.81
Q3	1.26	1.98	1.16
Maximum	15.63	9.60	4.60

Table XLI: High energy density 90° orientation dendrite area, length, and breadth statistics for the ‘Z’ sample.

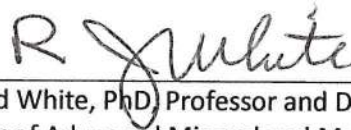
187.6 J/mm ³ 90° Dendrite Size 'Z'			
Statistic	Area(μm ²)	Length(μm)	Breadth(μm)
Counts (No Units)	92326	92326	92326
Mean	0.55	1.21	0.65
Standard Deviation	0.29	0.37	0.20
Coefficient of Variation	1.90	3.28	3.32
Minimum	0.14	0.58	0.29
Q1	0.34	0.93	0.52
Median	0.49	1.16	0.58
Q3	0.71	1.40	0.80
Maximum	1.81	2.27	1.28

SIGNATURE PAGE

This is to certify that the thesis prepared by Steven Keckler entitled "Material Properties of Laser Powder Bed Fusion Processed 316L stainless Steel" has been examined and approved for acceptance by the Department of Metallurgical and Materials Engineering, Montana Tech of The University of Montana, on this 20th day of July, 2018.



K.V. Sudhakar, PhD, Associate Professor
Department of Metallurgical and Materials Engineering
Chair, Examination Committee



Ronald White, PhD, Professor and Director
Center of Advanced Mineral and Metallurgical Processing
Member, Examination Committee



Bruce Madigan, PhD, Professor and Department Head
Department of General Engineering
Member, Examination Committee



Ronda Coghill, MS, Researcher II
Center of Advanced Mineral and Metallurgical Processing
Member, Examination Committee